Spatial and temporal seasonal trends in coastal upwelling off Northwest Africa, 1981–2012

Thomas E. Cropper *, Edward Hanna, Grant R. Bigg

Department of Geography, University of Sheffield, Winter Street, Sheffield, S10 2TN, UK

ABSTRACT

Seasonal coastal upwelling was analyzed along the NW African coastline (11–35°N) from 1981 to 2012. Upwelling magnitudes are calculated by wind speed indices, sea-surface temperature indices and inferred from meteorological station, sea-surface height and vertical water column transport data. A permanent annual upwelling regime is documented across 21–35°N and a seasonal regime across 12–19°N, in accordance with the climatology of previous studies. Upwelling regions were split into three zones: (1) the Mauritania–Senegalese upwelling zone (12–19°N), (2) the strong permanent annual upwelling zone (21–26°N) and (3) the weak permanent upwelling zone (26–35°N). We find compelling evidence in our various indices for the Bakun upwelling intensification hypothesis due to a significant coastal summer wind speed increase, resulting in an increase in upwelling-favorable wind speeds north of 20°N and an increase in downwelling-favorable winds south of 20°N. The North Atlantic Oscillation plays a leading role in modifying interannual variability during the other seasons (autumn–spring), with its influence dominating in winter. The East Atlantic pattern shows a strong correlation with upwelling during spring, while El Niño Southern Oscillation and Atlantic Multi-decadal Oscillation teleconnections were not found. A disagreement between observationally-based wind speed products and reanalysis-derived data is explored. A modification to the Bakun upwelling intensification hypothesis for NW Africa is presented, which accounts for the latitudinal divide in summer wind regimes.

© 2014 The Authors. Published by Elsevier Ltd. Open access under CC BY license.

1. Introduction

The Canary Upwelling Ecosystem (CUE) situated off Northwest (NW) Africa (11–35°N, Fig. 1) is an important socio-economic, oceanographic and climatological region. The Canary Current itself is the eastern, southward flowing component of the North Atlantic Subtropical Gyre and is one of the major coastal upwelling regions of the world, along with the Benguela (Hagen et al., 2001), Humboldt (Thiel et al., 2007) and California (Pérez-Brunius et al., 2007) eastern boundary upwelling ecosystems (EBUE). These EBUEs cover approximately 1% of the total ocean surface but account for over 20% of the global fish catch (Pauly and Christensen, 1995); therefore, monitoring changes across these regions is of the upmost importance, especially as a fisheries response to global climate change has recently been documented (Cheung et al., 2013; Payne, 2013).

For coastal upwelling to occur across NW Africa, three factors are required (Gómez-Gesteira et al., 2008): (1) persistent winds, (2) a solid boundary, and (3) the Coriolis effect. The consistent alongshore, equatorward direction of the trade winds along the majority of the

NW African coastline results in the deflection of oceanic water to the right, away from the coast (Ekman Transport). When this transported water is forced offshore at sufficient rates, mass balance is maintained by the upwelling of subsurface water from below (Sverdrup, 1938). Upwelled water is typically denser, cooler and richer in nutrients than surface waters and has significant impacts on coastal climates and marine biology (Miranda et al., 2012).

The 'Upwelling Intensification Hypothesis' (Bakun, 1990), later taken up by Diffenbaugh et al. (2004) and Bakun et al. (2010), suggested that, in a globally warming world, an increase in greenhouse gases will lead to a reduction in night-time continental cooling and an increase in daytime heating during the heating portions of the year (spring and summer for the NH subtropics). This would lead to an increased temperature gradient between land and ocean, which would intensify the continental–oceanic pressure gradient. Correspondingly, the alongshore wind stress would strengthen and drive an intensification of coastal upwelling. A considerable amount of literature has emerged since the original hypothesis, showing data and analysis for and against the upwelling intensification mechanism across the four main EBUEs and around the NW African coastline: we examine these contrasting findings below.
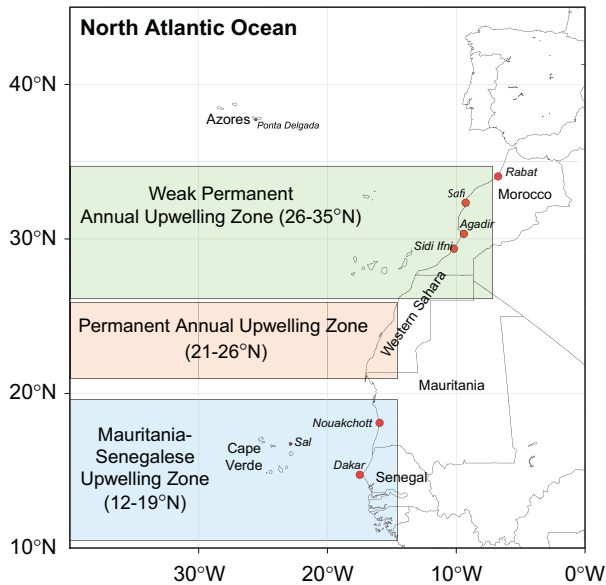
Fig. 1. The NW African upwelling region with the three upwelling zones (as described in Section 3.1) depicted. Also shown are the locations of Ponta Delgada, Azores and Sal, Cape Verde, which serve as the two nodes of the Trade Wind Index and the location of six coastal meteorological stations that are used for wind speed analysis (Section 3.3.1).

Maritime wind speed observations suffer from the unfortunate bias (usually towards stronger winds) of artificially increasing trends due to temporal inconsistencies in recording and archiving methods (Ramage, 1987; Cardone et al., 1990; Tokinaga and Xie, 2011a). To remove this problem, Bakun (1992) separately analyzed wind speed trends (during spring–summer) around the periphery of the North Atlantic Gyre in locations adjacent to and away from the areas where continental thermal lows develop. He concluded that the consistent positive trends in wind speed found near the continental thermal low areas and decreasing trends away from these areas are indicative of the upwelling intensification mechanism (but also realized the difficulty in separating the 'real' wind speed trend from the artificial one as both were long-term trends). Subsequently, several authors sought to analyze the spatial and temporal variations in upwelling via computer model approaches, sea surface temperatures (SST) and wind stress from satellite data, gridded datasets and paleo-sedimentary studies.

Hsieh and Boer (1992) ran the first model experiments (300–400-km grid resolution) under the explicit guise of determining future climate change impacts on the EBUEs. A doubling of atmospheric CO_2 in their study led to a decrease in coastal upwelling, primarily due to a relaxation of the trade winds because of a reduced equator–pole temperature gradient as a result of global warming. Mote and Mantua (2002) found little change in the magnitude and seasonality of upwelling across the four main EBUEs when comparing the 2080–2089 HadCM3 (300-km resolution) output to 1990–1999 observational wind stress. Conversely, it would appear that when a significantly higher spatial resolution is applied, model predictions of upwelling conform to the upwelling intensification hypothesis. Snyder et al. (2003) used a regional climate model at 40-km resolution and identified an increase in upwelling under double CO_2 scenarios across the California Current. Examining a combination of global (fifteen models at $\sim 2°$ resolution) and regional climate models (25 km resolution) under the IPCC A2 and B2 scenarios, Falvey and Garreaud (2009) discovered an intensification of upwelling (roughly a 15% increase for 2071–2100 relative to 1961–1990) across the Humboldt Current region, because of a 2–3 hPa increase in the Southern Hemisphere mid-latitude high-pressure systems.

Additionally, across the same time period under scenario A2, Miranda et al. (2012) used the Regional Ocean Modeling System (1/12° resolution) to identify an increase in upwelling frequency and magnitude across the Western Iberian Shelf, locally reducing the effect of global warming under this scenario. Thus, the current state of the literature suggests a strong scale-dependence in the modeling approach to quantifying upwelling that yields very contrasting results.

Published results regarding trend directions in upwelling across the NW African coastline are conflicting. Using Advanced Very High Resolution Radiometer (AVHRR) SST data from 1982 to 2001, Santos et al. (2005) identified a decadal shift in upwelling regime intensity off northwest Africa (22–30°N) around 1995–1996 lasting until 1999. During this short period, coastal SSTs decreased by roughly 0.7 °C and the meridional wind speed anomaly from the NCEP/NCAR reanalysis (Kalnay et al., 1996) across the same time period was enhanced by -0.7 ms^{-1} (a more negative value implies stronger equatorward meridional winds in the Northern Hemisphere). This relatively short 'shift' in conditions may represent the beginning of a regime change towards upwelling intensification but could also have been due to natural inter-annual variability. Subsequently, a paleo-sedimentary approach using two gravity cores from the Moroccan coastline (30.5°N, McGregor et al., 2007), found negative trends in alkenone-derived SST (-1 °C overall change). This suggested that twentieth century upwelling underwent a 'rapid' increase, consistent with meridional wind speed increases (-1 ms^{-1} during 1950–1992) in the ICOADS dataset (Woodruff et al., 2011) and positive trends in the Bakun (80 m^3 s^{-1} 100 m^{-1} across 1946–1981) and Pacific Fisheries Environment Laboratory (PFEL, 40 m^3 s^{-1} 100 m^{-1} across 1967-early 2000s) wind stress-derived upwelling indices (Schwing et al., 1996). Although the authors present a pertinent case for the upwelling intensification mechanism, there is the aforementioned caveat of the wind-speed sampling (Bakun et al., 2010; Tokinaga and Xie, 2011b) present in the ICOADS dataset and the potential for significant errors in the alkenone record (Herbert, 2001). Marcello et al. (2011) extended the SST analysis with AVHRR data up to 2006 (from 1987, across 13–32.5°N) and identified warming trends across the Northwest African coastline ranging from 1.0 to 3.3 °C for the 20-year period. However, relative to the warming rates across the open ocean along the same latitude, the values were much lower (greater) across 20–32.5°N (13–19°N): thus the authors surmised a relative increase (decrease) in coastal upwelling. A corresponding analysis (by the same authors) of scatterometer wind stress data (1992–2006) identified an increasing equatorward wind stress at Cape Ghir (30.4°N) and Cape Juby (27.5°N), again hinting at an increase in upwelling favorable conditions.

Narayan et al. (2010) highlighted a significant increase in the ICOADS and ERA-40 Reanalysis (Uppala et al., 2005) meridional wind stress across 28.5–33.5°N from 1960 to 2001 and 1958 to 2002 respectively in addition to a temperature reduction in their HadISST1 upwelling index (Rayner et al., 2003) from 1870 to 2001. However, the same authors identified a positive temperature trend in the latter part of the HadISST1 record [1960–2001] and a reduction in meridional wind stress from the NCEP/NCAR reanalysis [1960–2001] indicating a reduction in coastal upwelling. The study also considered basin-scale oscillations such as the North Atlantic Oscillation (NAO) and Atlantic Multidecadal Oscillation (AMO) but relationships with upwelling were ambiguous. Pardo et al. (2011) studied the CUE in detail using the NCEP/NCAR reanalysis and found a decrease in upwelling intensity from 1970–2009 in both wind stress and SST upwelling indices as well as discovering significant correlations with the NAO and the AMO (an r^2 value of approximately 0.3, dependent on latitude). Additionally, using the PFEL index, Gómez-Gesteira et al. (2008) discovered a decreasing trend in upwelling strength (a 45% (20%) decrease for April–September (October–March)) across 20–32°N

from 1967–2006. Finally, Santos et al. (2012), using AVHRR data, (1982–2010) demonstrated the prominence of coastal upwelling across 22–33°N by showing the regular lower magnitude of coastal, compared to open ocean, warming (except across 28–31°N). However, they acknowledged a lack of significant positive trend in summer (MJJAS) upwelling (using the NCEP/NCAR dataset) and found a significant correlation at a 1-year lag with the extended winter East Atlantic (EA) pattern.

The SST and wind stress derived methods of quantifying upwelling, mentioned above, are not without their caveats. SST derived estimates (hereafter, $UI^{\Delta SST}$) are typically the difference between SST at the coast and SST in the open ocean (usually a distance of 5° latitude). The main disadvantage of using this method is that changes in SST gradient between both the coast and the open ocean cannot be directly attributed to coastal upwelling. External factors such as freshwater input from local river discharge, macroscopic air–sea interactions, synoptic-scale weather systems and the variable oceanic mixed-layer depth can all influence SSTs. For example, a reduction in surface mixing across the open ocean could result in a shallower mixed layer that is readily susceptible to solar warming (Narayan et al., 2010). The increased ocean temperature in this scenario would impact the SST gradient and indicate an upwelling increase in $UI^{\Delta SST}$. Nevertheless, $UI^{\Delta SST}$ has widespread application and has been shown to correspond spatially and temporally well with wind stress-derived estimates, although usually at a time lag of 0–3 months (Nykjaer and Van Camp, 1994; Santos et al., 2012).

Wind stress derived upwelling (hereafter, UI^W), as found in numerous upwelling studies (Gómez-Gesteira et al., 2006, 2008; Santos et al., 2012), represents the (estimated) potential effects of wind stress on the ocean surface. At the coastal grid box scale, the UI^W effectively integrates the coastal boundary-associated Ekman divergence and the Ekman divergence due to cyclonic wind stress curl (Bakun and Nelson, 1991; Bakun and Agostini, 2001). Some studies, given sufficiently high spatial resolution datasets, have separated Ekman divergence components into the wind stress-derived 'Ekman transport' and the wind stress curl derived 'Ekman pumping' (Pickett and Paduan, 2003; Castelao and Barth, 2006). However, (given the variable scales of grid box size from the numerous data sets we use in this study) the UI^W alone should be sufficient for the spatial-temporal trend analysis goals of this paper. Finally, the UI^W is parameterized and makes certain assumptions, but still, based on current understanding, represents a good approximation of Ekman transport (Schwing et al., 1996).

Previous studies have naturally combined the various methods of quantifying upwelling in an attempt to elucidate spatial and temporal changes. However, there is still a degree of conflicting evidence regarding current changes across the CUE that mainly correspond to: (1) the way in which SST or wind data are obtained, via either in situ observations, satellites or reanalysis; (2) the exact spatial regions and temporal periods (intra- and inter-annual) considered; and (3) how upwelling estimates are analyzed on an intra-annual basis, given that the intensification mechanism is not expected to operate all year round.

Bakun et al. (2010) recognized the need for further useful supporting time series in quantifying upwelling trends and demonstrated the use of atmospheric water vapor as a beneficial proxy variable in relation to upwelling trends off the coast of Peru. Their two water vapor time series (precipitable water and total column water vapor from the NCEP/NCAR and ERA-40 reanalyses respectively) correlated significantly with their upwelling estimates (typical r values in the range of 0.3–0.5 ($p < 0.05$) across most seasons). Their theory was that as the most important greenhouse gas, water vapor enhances the local radiative heating cycle and serves to augment the upwelling intensification mechanism even if the mesoscale winds slacken. Across the

Humboldt region, the main driver of inter-annual climate variability, the El Niño Southern Oscillation (ENSO), is traditionally associated (during the El Niño phase) with a reduction of coastal wind speeds (Huyer et al., 1987), but also, with increases in atmospheric water vapor. As such, coastal wind speeds could increase even if the synoptic conditions favor a decrease. This highlights a potential scale-dependence on coastal upwelling wind speeds between large-scale and local processes, which could both significantly change under global warming (Miranda et al., 2012).

Following the same logic as Bakun et al. (2010), upwelling signals should also be detectable in previously lesser-considered, yet widely available, atmosphere and ocean datasets. Here, in addition to comparing a wide range of datasets using the $UI^{\Delta SST}$ and UI^W methods (Sections 2.1 and 2.2), we additionally analyze wind speed from coastal land-based meteorological stations (Section 2.3), sea surface height variability from satellite altimetry and ocean reanalysis (SSH, Section 2.4), and vertical water column velocity (VWCV, Section 2.5), and we also consider the influence of basin-scale climate indices.

Our overriding aim was to test if the upwelling intensification hypothesis is evident in current records across the CUE. Additionally, the purpose of this study was to

1. Examine the variability between various UI^W indices to determine if there are any significant differences between the datasets;
2. Determine if lesser-used indicators of upwelling agree with these indices, to further elucidate any temporal and spatial trends;
3. Place an emphasis on seasonal trends (the intensification hypothesis should mainly apply during boreal summer (JJA)) and the importance of basin-scale oscillations on interannual variability.

2. Data and methods

The CUE is defined here as 11–35°N (Fig. 1). Supplementary Table 1 lists all the data and sources we use in this paper. All time series are created as, or aggregated to, monthly temporal resolution, then converted to seasonal resolution for analysis. Spatial resolutions are dependent on the original datasets, and we consider the common temporal period of 1981–2012.

2.1. Wind stress upwelling indices

To adequately cover the range of previously used UI^W indices by other authors and compare different observational and reanalysis sources across our selected time period, we use seven different sources to calculate the UI^W. These are (1) the NCEP/DOE II Reanalysis (Kanamitsu et al., 2002); (2) the ERA-Interim Reanalysis (ERA-I, Dee et al., 2011); (3) the PFEL upwelling index (http://las.pfeg.noaa.gov); (4) the Twentieth Century Reanalysis Project (20CR, Compo et al., 2011); (5) the International Comprehensive Ocean-Atmosphere Dataset (ICOADS, Woodruff et al., 2011); (6) the NASA MERRA Reanalysis (MERRA, Rienecker et al., 2011); and (7) the Climate Forecast System Reanalysis (CFSR, Saha et al., 2010). Wave and Anemometer based Sea-Surface Wind (WASWind, Tokinaga and Xie, 2011b) and scatterometer-derived winds (SeaWinds, Lungu et al., 2006) are used later in the article as supporting indices. Monthly zonal and meridional wind speeds were extracted from all sources at 10-m height.

To calculate the upwelling index (Borja et al., 1996; Gómez-Gesteira et al., 2006; Santos et al., 2012) the Ekman transport (Q) is

derived from the wind stress (τ) fields. Firstly, the zonal (τ_x) and meridional (τ_y) components of wind stress are calculated from the wind speeds ($W=(W_x, W_y)$), as

$$\tau_x = \rho_a C_d (W_x^2 + W_y^2)^{1/2} W_x \text{ and } \tau_y = \rho_a C_d (W_x^2 + W_y^2)^{1/2} W_y \quad (1)$$

then,

$$Q_x = \frac{\tau_y}{\rho_w f} \text{ and } Q_y = \frac{-\tau_x}{\rho_w f} \quad (2)$$

where ρ_a is the air density (1.22 kg m^{-3}), ρ_w the sea water density (1025 kg m^{-3}) and C_d the dimensionless drag coefficient, typically 1.3×10^{-3} (Schwing et al., 1996). The Coriolis parameter, f, is defined as twice the component of the angular velocity of the earth, Ω, at latitude θ ($f = 2\Omega \sin(\theta)$, where $\Omega = 7.292 \times 10^{-5}$ s^{-1}). In turn, the UI^W can then be calculated as

$$UI^W = -\sin(\varphi - \pi/2)Q_x + \cos(\varphi - \pi/2)Q_y \quad (3)$$

where φ is the mean angle between the shoreline and the equator. Using this index, positive (negative) values correspond to upwelling (downwelling) favorable conditions. Whilst highly irregular on smaller scales, the northwest African coastline angle can macroscopically be classed as 55° from 21°N to 36°N, 90° from 12°N to 21°N and 120° from 10°N to 12°N relative to the equator. The data points for the UI^W transects along the northwest African coastline are the closest full ocean grid-box to the coast (so as not to influence the drag coefficient). Due to the reduced Coriolis effect closer to the equator, upwelling estimates for the lower latitudes (below ~20°N) are probably biased slightly high.

2.2. SST upwelling indices

We use three different datasets to calculate the UI$^{\Delta SST}$: (1) the Hadley Center Sea Ice and Sea Surface Temperature dataset (HadISST1, Rayner et al., 2003); (2) the ICOADS SST; and (3) the Reynolds SST v2 dataset (OISST, Reynolds et al., 2007). The UI$^{\Delta SST}$ at each latitudinal point is defined as the difference in SST between the coast and the ocean:

$$UI^{\Delta SST} = SST coast - SST ocean \quad (4)$$

where $SST coast$ is the SST of the closest grid box to the coast and $SST ocean$ is the SST of the grid box along the same latitude that is 5° further west. Therefore, an increase (decrease) in the UI$^{\Delta SST}$ is equivalent to a decrease (increase) in upwelling intensity.

2.3. Meteorological data

We use wind-speed data from six meteorological stations situated along the NW African coastline (Table 1, Fig. 1) from the National Climatic Data Centre's Global Summary of the Day (GSOD) network (ncdc.noaa.gov). We also use the normalized sea-level-pressure (SLP) difference between meteorological stations from the Azores and Cape Verde (Fig. 1) as a proxy for the strength of the NE Atlantic trade winds (Trade Wind Index, TWI),

after Cropper and Hanna (in press). This index does not suffer from the sampling bias that affects maritime wind speed observations. All of the stations were tested for homogeneity using the Pettitt (Pettitt, 1979), Buishand and Standard Normal Homogeneity Test (Buishand, 1982; Alexanderson, 1986). Station metadata were not available, however identification of breaks was relatively straight-forward when the test results corresponded to, or near-to, gaps in the time series that are accompanied by clear shifts in the mean (for times of adjustments, see Table 1).

2.4. Sea-surface height

Under upwelling conditions, alongshore winds transport water offshore. As such, the SSH near the coast should experience a detectable reduction (the greater density of upwelled water from depth should further augment the SSH reduction). There are no continuous long-term tide-gauge data along the Northwest African coastline, from either the Permanent Mean Service for Sea Level (http://www.psmsl.org) or the Joint Archive for Sea Level (http://ilikai.soest.hawaii.edu/UHSLC/jasl.html). Therefore we examined the mean sea level anomaly (MSLA) obtained via satellite altimetry from the TOPEX/Poseidon, Jason-1, ERS and Envisat missions. We use three realizations of this data: (1) the Church and White (2011) dataset (with the inverse barometer and glacial isostatic correction applied); (2) the delayed time Ssalto/ Duacs product directly from the Archiving, Validation and Inter- pretation of Satellite Oceanographic Data (AVISO) homepage (similar corrections applied); and (3) the Aviso/Niiler Climatology dataset (Table S1). Additionally, we analyzed several ocean reana- lysis datasets, which assimilate the altimetry data: (1) the Global Ocean Data Assimilation System (GODAS, Behringer and Xue, 2004); (2) the Simple Ocean Data Analysis v2.1.6 (SODA, Carton and Giese, 2008); and (3) the Operational Ocean System Reanalysis 4 (ORSA4, Balmaseda et al., 2013). Our reason for this latter analysis was that, as the altimetry signal close to the coast deteriorates within approximately 40 km of the coastline (e.g. Saraceno et al., 2008), the SSH values in the closest coastal grid box may not necessarily be an entirely accurate representation of the coastal SSH. Therefore, the effect on SSH due to upwelling (or other influences) may be lost. The fine resolution of the SODA, GODAS and AVISO datasets, may, however, allow coastal SSH changes to be captured.

2.5. Vertical water column velocity

We use the geometric vertical velocity from the GODAS dataset at 50 m depth. This variable is used as a direct upwelling estimate across the NW American coastline by the Climate Prediction Centre (http:// www.cpc.ncep.noaa.gov/products/GODAS/coastal_upwelling.shtml) and measures the Ekman pumping/suction 'component' of the upwel- ling process (so effectively integrates both the coastal-boundary wind stress and open ocean wind stress curl Ekman divergence effects).

Table 1
Coastal meteorological station data used in this study (coordinates expressed as decimal degrees).

Meteorological Wind Speed Stations						
Station	Country	Temporal extent	Latitude (N)	Longitude (W)	Distance from coast (km)	Homogeneity adjustments
Rabat	Morocco	1973–2013	34.05	06.75	4	October 1986, November 1992
Safi	Morocco	1973–2013	32.34	09.27	1	June 1989, October 2004
Agadir	Morocco	1992–2013	30.33	09.41	20	
Sidi Ifni	Morocco	1973–2013	29.37	10.18	1	April 1992, October 2000
Nouakchott	Mauritania	1973–2013	18.10	15.95	5	July 1989
Dakar	Senegal	1973–2013	14.74	17.49	2	December 1987, May, June 1992

2.6. Basin-scale climate oscillations

The following climate indices are used in this study (Table S2):

1. The North Atlantic Oscillation Index (NAO). We use two separate versions of the indices – the extended station based Azores–Iceland pressure difference (Cropper and Hanna, in press) and the leading principal component (PC) of an Empirical Orthogonal Function Analysis (EOF) of SLP throughout all months across 25°–75°N, 90°W–30°E (using data from the NCEP-NCAR reanalysis). The latter may be more suited to capturing the variability of the oscillation across the summer months, whereas the former is a better general indicator of changes in the Azores High;
2. The East-Atlantic Pattern (EA, Barnston and Livezey, 1987), a 'southward-shifted' NAO pattern representing the second mode of low-frequency SLP variability across the North Atlantic. We use the Climate Prediction Centre's (CPC) index (Table S2);
3. The Atlantic Multidecadal Oscillation (AMO), defined here as the area-averaged, detrended, north Atlantic (25°N–60°N, 7°W–75°W) SST anomalies minus the regression of the SST on the global mean temperature after the methodology of van Oldenborgh et al. (2009) (using HadSST2 data);
4. The Multivariate Niño Index (MEI, Wolter and Timlin, 2011);
5. The TWI discussed in Section 2.3 (Cropper and Hanna, in press).

Lagged correlations – intra-annually (at a monthly and seasonal resolution) up to 1 year and inter-annually (yearly resolution of seasonal values) up to 10 years – were considered as well as standard correlation analysis between the climate oscillations and the various measures of upwelling.

2.7. Trend analysis

We use seasonal averages of the various upwelling indices from 1981 to 2012, focusing primarily on summer (JJA), as this is the season where an oceanic–continental pressure gradient should be strongest. For determining trend rates we use ordinary least squares regression. Whilst we propose that there is no mechanism by which upwelling values from one season could influence the same season the year after, some of the upwelling time series display traits of statistical dependence, i.e. autocorrelation, which spuriously affects significance estimates of the trendline (Santer et al., 2000). To counteract this, for each time series we take the autocorrelation (ϕ) of the residuals of the trend estimate and apply corrections to the standard error (SE) and effective degrees of freedom (DF) based on the structure of the autocorrelogram.

If, at lag-1, the residuals display no significant autocorrelation then we make no adjustments to the SE and DF; however if the lag-1 autocorrelation (r_1) is significant, we assume the data follow a first order autoregressive AR(1) structure. To account for this we firstly adjust the effective DF so that our adjusted degrees of freedom $DF_{adjusted}$ based on the number of data points n is

$$DF_{adjusted} = n\left(\frac{1-r_1}{1+r_1}\right) \tag{5}$$

We then adjust the standard error by assuming a number of data per effective degree of freedom under an AR(1) process (as in Foster and Rahmstorf (2011)), which is given as

$$k = \left(\frac{1+\phi}{1-\phi}\right) \tag{6}$$

Here (ϕ) is the lag-1 value of the time series autocorrelation (r_1). Then, the square root of k is then multiplied by the original

standard error to give the adjusted standard error:

$$SE_{adjusted} = SE\sqrt{k} \tag{7}$$

The $SE_{adjusted}$ then replaces the original SE in the Student's t test, and the $DF_{adjusted}$ taken into account when determining significance. However, sometimes the autocorrelation structure is more pronounced, i.e., it differs from a typical AR(1) process (which assumes an exponential decay) and there is still significant autocorrelation in the residuals of the trend estimate at or beyond lag-2. When this occurs we apply corrections to the SE as if the residuals we structured as an ARIMA(1,1) process, which changes the estimated number of data per effective degrees of freedom to

$$k = 1 + \frac{2r_1}{(1-\phi)} \tag{8}$$

where the autocorrelation (ϕ) is taken as

$$\phi = \frac{r_2}{r_1} \tag{9}$$

and ϕ from Eq. (9) replaces r_1 in Eq. (5). For robustness we repeat trend estimates using the Thiel–Sen regression and modified Mann–Kendall trend test (Hamed and Rao, 1998), finding almost identical trend magnitudes and significances. We find that the $UI^{\Delta SST}$ time series display traits of autocorrelation more frequently than the other indices, with the latter having residuals that are more independently distributed.

3. Results

3.1. Seasonal upwelling cycle

Fig. 2 illustrates the mean annual cycle of upwelling for the seven UI^W and three $UI^{\Delta SST}$ indices. The general pattern is reflected well in all ten UI (note the reversed color scheme for the $UI^{\Delta SST}$). The area of intense, permanent annual upwelling (21–26°N) is well captured by all ten indices. Upwelling appears to be a permanent annual phenomenon up to ~33°N – although a small zone around ~30°N near Cape Ghir (where the coastline inverts relative to its macroscopic orientation) appears to have much weaker upwelling compared to the surrounding latitudes. The seasonal pattern of upwelling differs slightly between the UI^W and the $UI^{\Delta SST}$, with the $UI^{\Delta SST}$ generally lagging the UI^W signal by 0–2 months, as previously found here by Nykjaer and Van Camp (1994). South of 20°N, a downwelling regime is present between March and October (UI^W) or May and November ($UI^{\Delta SST}$). Based on the obvious latitudinal divides, and reinforced by covariance analysis between the upwelling grid boxes (not shown), we characterize the CUE upwelling into three meridionally averaged zones (weighted by latitude, and shown on Fig. 1):

1. 12–19°N – Mauritania–Senegalese upwelling zone. Upwelling occurs during the winter months and fades during the summer months, related to the seasonal migration of the trade winds;
2. 21–26°N – Strong permanent annual upwelling zone;
3. 26–35°N – Weak permanent annual upwelling zone. Upwelling is typically a year-round occurrence, but its magnitude is weaker than in the permanent upwelling zone. Stronger upwelling is present in summer, associated with the trade-wind migration.

Fig. 3 illustrates the mean annual cycle and monthly standard deviation of each of these three zones for each UI, allowing a more direct comparison between the UI magnitudes. Across the strong permanent upwelling zone (21–26°N), the annual range is much lower than that of the lower latitudes (12–19°N); however, monthly variability (signified by the 1σ bars) is generally higher. Across the
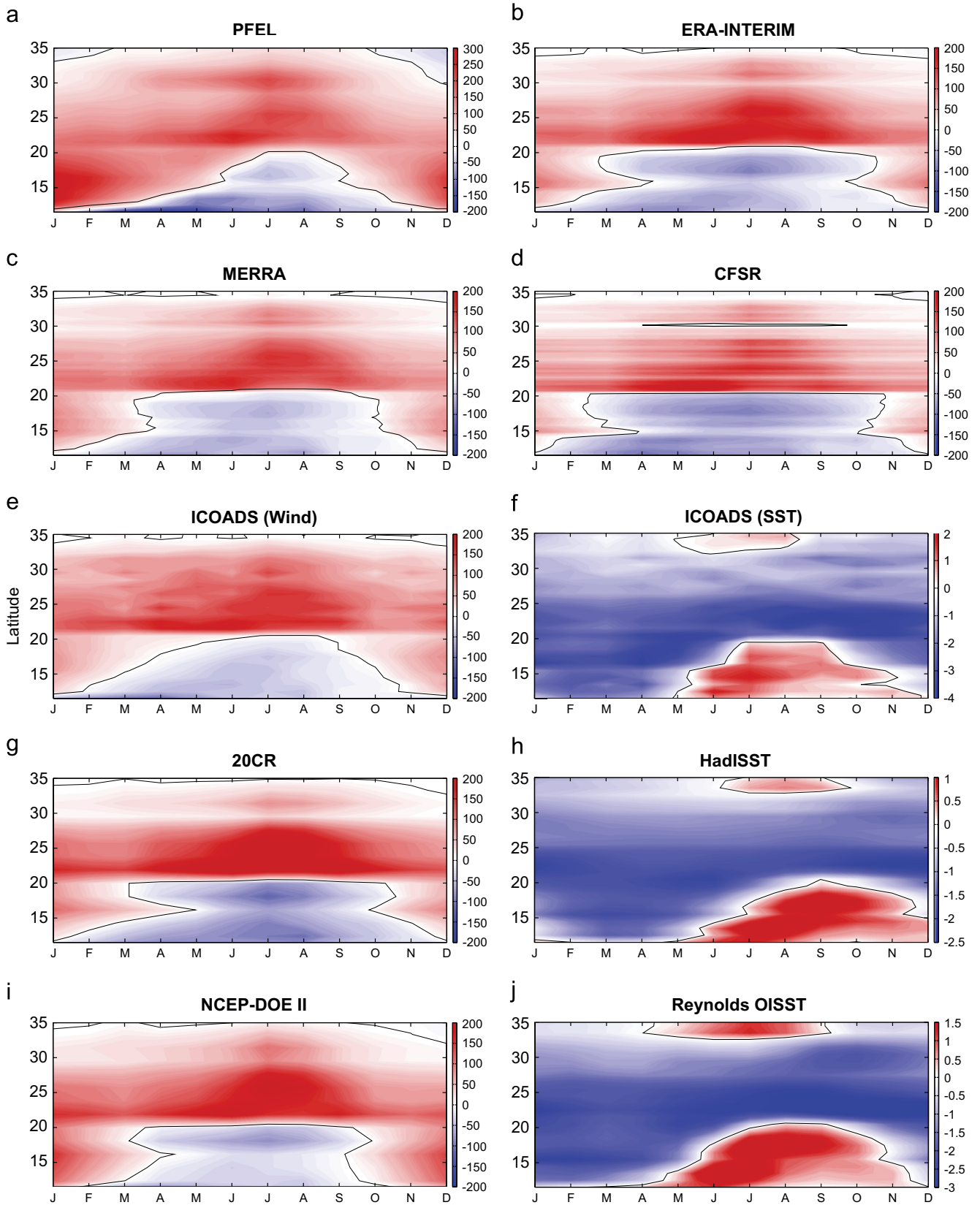
Fig. 2. The 1981–2012 climatology of our seven UI^W (units: m^3 s^{-1} 100 m^{-1}) and three UI$^{\Delta SST}$ (units: °C) indices. Black contours indicate the divide between upwelling and downwelling favorable conditions. For the UI^W, red (blue) corresponds to upwelling (downwelling) conditions and the opposite applies for the UI$^{\Delta SST}$. (For interpretation of the references to color in this figure legend, the reader is referred to the web version of this article.)

weak permanent upwelling zone (26–35°N), upwelling averages around 50 m^3 s^{-1} 100 m under the UI^W or -1 °C under the UI$^{\Delta SST}$ with a modest seasonal cycle that peaks in summer. A similar

pattern is evident across the strong permanent upwelling zone (21–26°N), with winter values ranging between 75–130 m^3 s^{-1} 100 m and summer values between 130–200 m^3 s^{-1} 100 m.
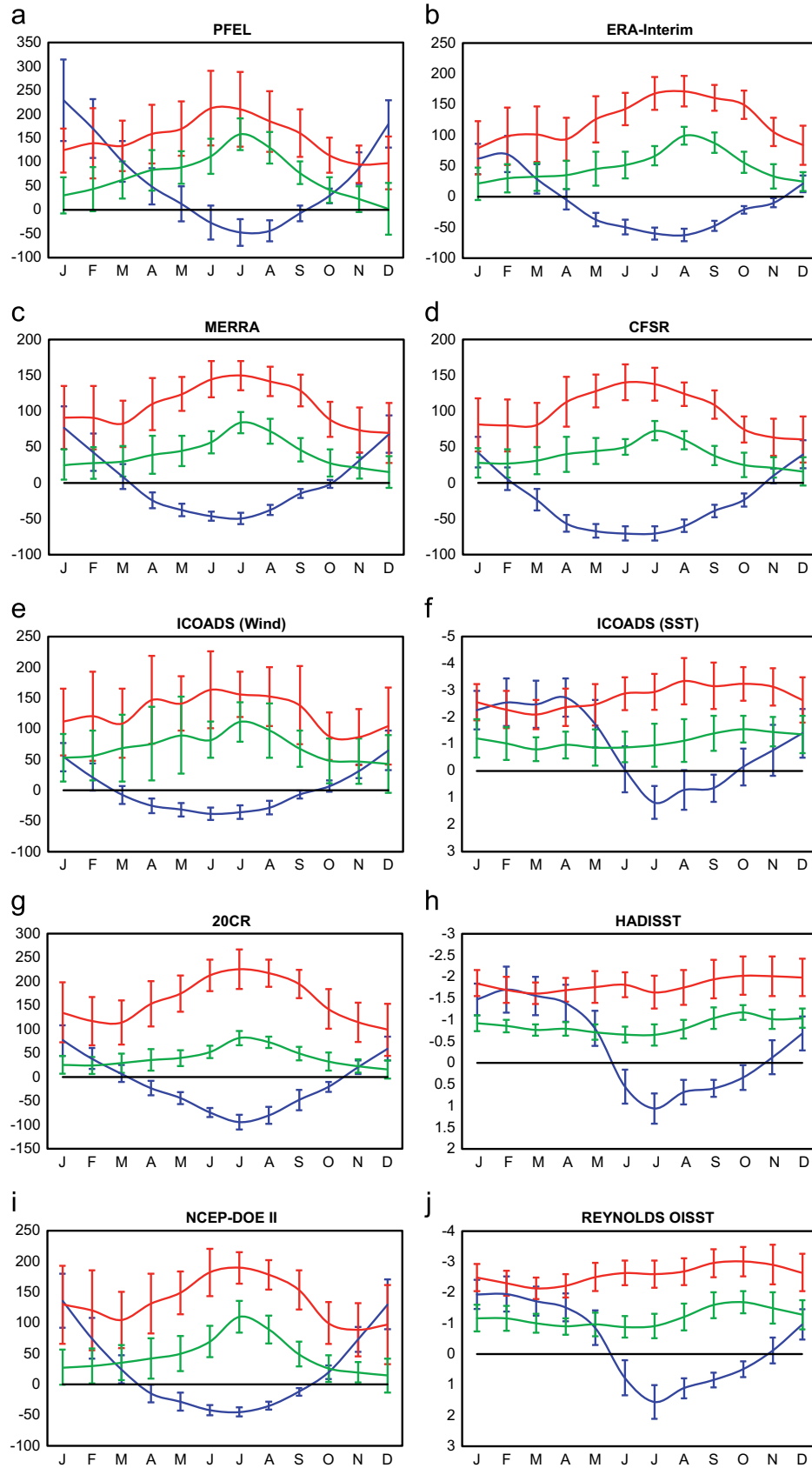
Fig. 3. The monthly climatology (1981–2010) for the Mauritania–Senegalese upwelling zone (12–19°N, blue line), permanent upwelling zone (21–26°N, red line) and the weak permanent upwelling zone (26–35°N, green line) for the seven UI^W (units: $m^3\ s^{-1}\ 100\ m^{-1}$) and three $UI^{\Delta SST}$ (units: °C) indices. Error bars on the individual months highlight the (1σ) monthly variability. (For interpretation of the references to color in this figure legend, the reader is referred to the web version of this article.)

Across the Mauritania–Senegalese upwelling zone (12–19°N) down-welling during the summer months typically averages around $-50 \, m^3 \, s^{-1}$ 100 m or 1 °C respectively and the winter upwelling varies in strength (~200 and $\sim150 \, m^3 \, s^{-1}$ 100 m for the PFEL and NCEP-DOE data respectively, compared to an average of around 50–75 $m^3 \, s^{-1}$ 100 m for the other five UI^W).

The three $UI^{\Delta SST}$ indices are strongly correlated with each other across their latitudinal zones with typical r-values of 0.8–1.0 (applied to detrended, annual data, but these correlations remain strong only if individual months and/or various temporal periods are considered), a similar trait shared by the six UI^W indices ($r=0.7$–1.0). However, correlations between the $UI^{\Delta SST}$ and UI^W indices are generally ambiguous, unless, as in Nykjaer and Van Camp (1994) time lags are applied (which latitudinally vary and are strongest when UI^W leads by between 0 and 2 months).

3.2. Interannual upwelling evolution

Fig. 4 displays the evolution of summer upwelling from 1981 to 2012 for all ten UI spread across the three spatially defined upwelling zones. A prominent feature of the two higher-latitude zones (21–35°N) is a progressive increase during the 1990s, followed by a short-lived negative trend which lasts from 2000 until around 2004/5 which is followed in turn by a strong positive increase across most indices (the reanalysis-derived UI^W stay constant whereas the observationally derived UI^W (PFEL and ICOADS) rise across 21–26°N). Additionally, the PFEL and ICOADS UI^W experience a decrease in upwelling across the Mauritania–Senegalese Zone whereas the reanalysis UI appear to exhibit little change. Table 2 illustrates the seasonal trends in upwelling for the main seven UI^W (and WASWind) and three $UI^{\Delta SST}$ from 1981–2012 for the three specific latitudinal zones (a few indices do not fully extend to 2012, Supplementary Table 1). Focusing again on summer trends first – a general tendency towards a decrease in upwelling is found across the Mauritania–Senegalese (12–19°N) upwelling zone, indicated by statistically significant reductions in the PFEL, ICOADS and CFSR UI^W indices and a significant increase in the OISST $UI^{\Delta SST}$. Confidence intervals for the other indices exceed the trend values and are not significant except the NCEP-DOE UI^W, which suggests a small positive upwelling increase (Table 2). Across the permanent upwelling zone (21–26°N), significant increases in upwelling are shown in the PFEL, ICOADS UI^W, NCEP-DOE, OISST and HadISST indices. Across the weak permanent upwelling zone (26–35°N), there is a positive tendency towards enhanced upwelling in every UI (except ICOADS $UI^{\Delta SST}$), although these trends are only significant for the ICOADS UI^W, NCEP-DOE and OISST indices.

The general tendency across summer appears to be one of an increase in upwelling-favorable winds north of 21°N and increase in downwelling-favorable winds south of 19°N. The $UI^{\Delta SST}$ trends show support for this observation (Fig. 4), although the strong interannual variability of SST affects the signal. If we consider the widespread spatial patterns in meridional wind speed and SST trends (Fig. 5b–h), we find further support for this. Typically, increased negative trends in meridional wind speed (that vary in their spatial significance dependent on the dataset) can be identified across the northwest African coastline from around 35°N down to ~20–25°N and positive trends from around the equator (but always west of the Gulf of Guinea) to 20°N. Additionally, isolated sections of negative SST trends adjacent to Western Sahara and Southern Morocco (21–30°N, Fig. 5g–h) are surrounded by statistically significant open ocean warming regions.

Trends in winter upwelling variability are strongly correlated with the NAO (Fig. 6; Table 3). The correlations between the winter NAO and the various UI^W indices are significant for nearly every UI^W, even as far south as the Mauritania–Senegalese upwelling zone, but the relationship is weaker than across the more northerly upwelling zones. The average correlation coefficient between the station-based winter NAO and the three latitudinal zones ranges from 0.50 (12–19°N) to 0.59 (21–26°N), to 0.74 (26–35°N). The NAO/UI^W relationship remains strong during autumn (Supplementary Table 3c). During spring (Supplementary Table 3a), the NAO/UI^W relationship also remains strong (except across the permanent upwelling zone); however, for 21–35°N the EA pattern emerges as an important variable, significantly correlating with the NCEP-DOE II, MERRA, CFSR, 20CR and WASWind UI^W. During summer (Supplementary Table 3b), only the EA pattern across 26–35°N consistently appears as a significant correlation (with the PFEL, NCEP-DOE II, CFSR and 20CR UI^W), although its realistic summer impact is likely to be very limited (Barnston and Livezey, 1987).

Direct correlations between the (linearly detrended) seasonal upwelling indices and the seasonal AMO and ENSO are generally ambiguous, although the correlation tables do not display the effect of lag times or account for the potential low-frequency response of the oscillations. Generally, we would expect the NAO and EA to have an instantaneous/short lag effect on upwelling (when considering monthly/seasonal temporal scales), and find no evidence of temporal lags increasing the correlation strength (except for the $UI^{\Delta SST}$, which is known to generally lag the wind based indices by 0–2 months). Of particular interest are the lagged correlations (on the order of 0–9 months) between ENSO and our UI indices, seen as the ENSO mode typically initiates around April–June, and peaks during the autumn/winter months, with potential lags around the eastern Atlantic/African sector varying from 0 to 9 months (An and Wang, 2001; Wang and Enfield, 2002). However, we find no evidence for a significant ENSO contribution, across all our various UI indices at either monthly or seasonal timescales. The potential influence of the AMO on upwelling variability is discussed in Section 4.

3.3. Upwelling 'Proxy' indices

3.3.1. Wind speed

Unfortunately, there is a lack of quality station-based data along the NW African coastline. There is a large gap in the location of (coastal) meteorological stations between 21°N and 29°N (Fig. 1) which covers most of the major summer upwelling region. Regardless of this, summer trends in wind speed from six available coastal stations are presented (Table 1, Fig. 7). A positive trend is seen at four out of the six stations, but this is only significant at Safi (32.3°N). However, the trends at Agadir and Nouakchott also significant ($p < 0.1$) if outlier values (1992 and 1995 for Agadir, 1986 for Nouakchott) are removed.

An alternative method exists to characterize meridional/trade wind strength across the NE Atlantic sector based on the normalized SLP difference between the Azores and Cape Verde. Theoretically, an increased pressure difference between these two locations (the semi-permanent Azores high and the relatively lower pressure across Cape Verde) would result in greater wind speeds. This Trade Wind Index (TWI) has been shown to display a strong relationship with wind speeds across northwest Africa (Cropper and Hanna, in press) and has been increasing since 1973 (Fig. 8). The regression of the index onto the meridional wind speed field from the CFSR reanalysis highlights an equator-ward (poleward) meridional wind speed relationship north of (south of) ~21°N, although this is not significant across the entire coastal region (just the permanent annual upwelling zone). However, the positive trend in the TWI would seem to point to stronger large-scale meridional wind speeds across the upwelling regions (Fig. 8b).
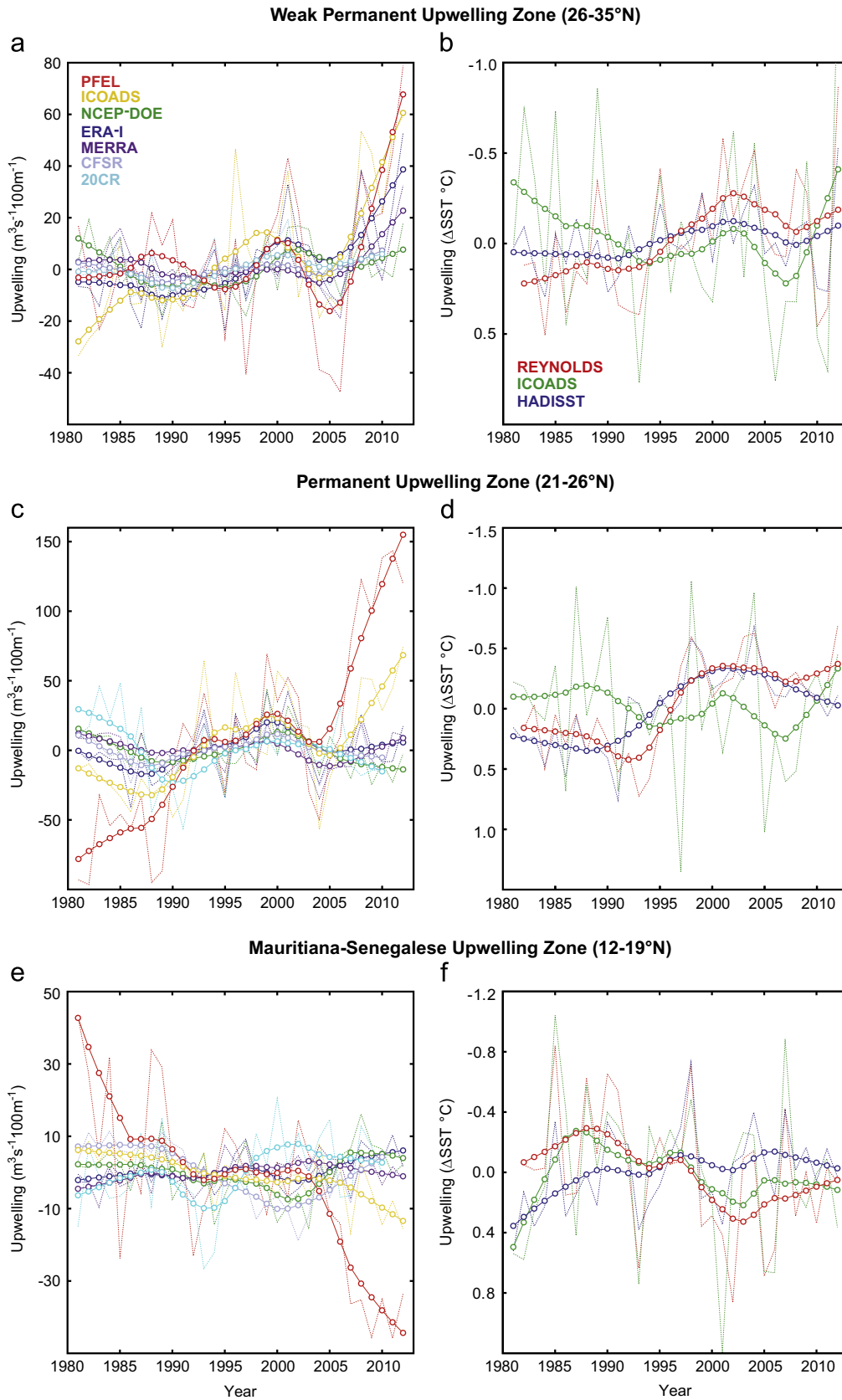
Fig. 4. Temporal evolution of the (a, c, and e) seven UI^W and (b, d, aand f) three UI$^{\Delta SST}$ for summer (JJA) from 1981 to 2012 (anomalies relative to the 1981–2010 base period). Thin dotted lines indicate yearly values and circled bold lines are the 9-year loess trend for each individual UI.

3.3.2. Vertical water column velocity

The VWCV variable from the GODAS reanalysis shows a strong divide between upwelling and downwelling around 21°N for its summer climatology (Fig. 9a). Once more, the slightly weaker upwelling area around 30°N is readily identified. Summer trends across the three upwelling zones (Table 2) indicate a significant

Table 2
Seasonal decadal trend rates during 1981–2012 (or the longest temporal period available, see Table S1) for multiple Upwelling Index estimates and 'proxy' variables (SSH – sea surface height (Section 3.3.3) and VWCV – 50 m depth vertical water column motion). Italicized text, bold and bold italics correspond to significance levels of 90%, 95% and 99% respectively.

Variable	Indices	Units	Season											
			DJF			MAM			JJA			SON		
			12–19°N	21–26°N	21–26°N	12–19°N	21–26°N	26–35°N	12–19°N	21–26°N	26–35°N	12–19°N	21–26°N	26–35°N
UI^W	ICOADS	$m^3\ s^{-1}\ 100\ m^{-1}\ dec^{-1}$	5.5 ± 6.6	***24.8 ± 14.9***[a]	9.9 ± 10.7	−0.6 ± 2.9	**25.0 ± 11.6**[a]	14.1 ± 13.4[a]	**−5.0 ± 2.9**[a]	**22.4 ± 11.5**[a]	**17.9 ± 7.5**[a]	1.8 ± 1.9	***27.4 ± 11.6***[a]	**7.7 ± 7.1**[a]
UI^W	PFEL	$m^3\ s^{-1}\ 100\ m^{-1}\ dec^{-1}$	− **18.9 ± 16.8**[a]	14.1 ± 15.1	−3.0 ± 11.1	**−18.0 ± 7.7**[a]	***33.2 ± 12.7***[a]	2.2 ± 7.9	**−19.8 ± 6.7**[a]	***59.1 ± 27.5***[a]	7.9 ± 16.4	**−6.0 ± 5.6**[a]	***26.8 ± 9.7***[a]	−2.7 ± 6.2
UI^W	NCEP-DOE II	$m^3\ s^{-1}\ 100\ m^{-1}\ dec^{-1}$	−0.9 ± 10.0	2.8 ± 15.0	−2.7 ± 6.8	−0.4 ± 4.4	3.2 ± 9.5	2.7 ± 5.8	*1.8 ± 1.5*[a]	*6.3 ± 7.1*[a]	**11.0 ± 5.4**[a]	−0.3 ± 3.5	7.2 ± 9.7	−0.1 ± 4.2
UI^W	ERA-I	$m^3\ s^{-1}\ 100\ m^{-1}\ dec^{-1}$	−1.6 ± 5.5	−0.6 ± 9.2	0.8 ± 5.0	2.1 ± 4.3	−2.3 ± 8.4	0.2 ± 4.5	0.3 ± 2.9	−3.5 ± 5.8	1.4 ± 3.9	1.4 ± 1.9	−1.8 ± 5.2	−2.8 ± 3.8
UI^W	MERRA	$m^3\ s^{-1}\ 100\ m^{-1}\ dec^{-1}$	−6.1 ± 7.0	−4.7 ± 10.4	−1.5 ± 5.5	−0.1 ± 3.1	−2.4 ± 6.7	−0.3 ± 4.6	1.4 ± 1.7	−3.0 ± 5.1	1.9 ± 4.1	0.4 ± 2.0	2.7 ± 7.0	−0.8 ± 4.0
UI^W	CFSR	$m^3\ s^{-1}\ 100\ m^{-1}\ dec^{-1}$	−7.4 ± 4.6	−5.3 ± 8.7	−3.1 ± 5.4	**−6.2 ± 3.0**[a]	4.5 ± 6.8	1.8 ± 4.0	**−4.9 ± 4.6**[a]	0.8 ± 6.2	1.2 ± 3.2	−2.5 ± 4.5	4.7 ± 6.2	0.4 ± 3.7
UI^W	20CR	$m^3\ s^{-1}\ 100\ m^{-1}\ dec^{-1}$	−4.0 ± 7.2	− **14.7 ± 14.1**[a]	−3.3 ± 4.8	**−4.2 ± 3.8**[a]	1.7 ± 10.8	3.7 ± 4.3	3.9 ± 4.3	−5.7 ± 10.2	3.1 ± 3.5	***6.7 ± 3.7***[a]	−6.4 ± 9.8	−1.3 ± 4.0
UI^W	WASWind	$m^3\ s^{-1}\ 100\ m^{-1}\ dec^{-1}$	−1.2 ± 4.6	**−8.9 ± 7.9**[a]	−3.1 ± 6.2	2.4 ± 2.4	0.2 ± 5.3	1.2 ± 5.6	0.9 ± 2.4	−2.0 ± 4.9	2.5 ± 3.7	2.0 ± 1.8	1.0 ± 5.1	2.6 ± 4.4
$UI^{\Delta SST}$	OISST	$°C\ dec^{-1}$	**−0.15 ± 0.13**[a]	**−0.32 ± 0.23**[a]	**−0.25 ± 0.12**[a]	*0.14 ± 0.14*[a]	**−0.24 ± 0.15**[a]	**−0.13 ± 0.09**[a]	**0.16 ± 0.15**[a]	**−0.26 ± 0.20**[a]	**−0.15 ± 0.12**[a]	0.03 ± 0.09	***−0.37 ± 0.19***[a]	**−0.30 ± 0.18**[a]
$UI^{\Delta SST}$	HadISST	$°C\ dec^{-1}$	−0.06 ± 0.11	*−0.16 ± 0.15*[a]	−0.01 ± 0.06	**−0.15 ± 0.11**[a]	**−0.16 ± 0.12**[a]	0.01 ± 0.05	−0.10 ± 0.10	***−0.22 ± 0.10***[a]	−0.05 ± 0.07	***−0.16 ± 0.07***[a]	**−0.27 ± 0.12**[a]	**−0.08 ± 0.06**[a]
$UI^{\Delta SST}$	ICOADS	$°C\ dec^{-1}$	0.02 ± 0.24	−0.06 ± 0.26	0.02 ± 0.18	0.04 ± 0.20	−0.05 ± 0.19	*0.11 ± 0.11*[a]	0.04 ± 0.18	0.06 ± 0.21	0.06 ± 0.19	0.13 ± 0.19	0.08 ± 0.19	0.02 ± 0.11
SSH	AVISO (1)	$cm\ dec^{-1}$	3.1 ± 12.5	1.3 ± 15.4	−3.3 ± 12.7	−1.2 ± 8.6	−0.6 ± 9.9	−1.3 ± 11.6	−1.7 ± 14.5	3.8 ± 7.1	5.56 ± 7.69	1.7 ± 11.5	−1.0 ± 8.1	−0.3 ± 8.5
SSH	AVISO (2)	$cm\ dec^{-1}$	2.8 ± 8.2	5.2 ± 13.4	1.8 ± 13.1	0.4 ± 9.2	−0.2 ± 7.5	2.5 ± 9.8	5.6 ± 7.1	4.7 ± 8.6	5.9 ± 5.5	4.0 ± 7.5	5.9 ± 9	4.7 ± 6.3
SSH	AVISO (3)	$cm\ dec^{-1}$	6.6 ± 11.9	8.8 ± 18.4	6.9 ± 17.6	−0.6 ± 13.4	−0.8 ± 11.2	0.8 ± 14.3	5.6 ± 13.5	4.7 ± 12.4	5.5 ± 10.1	10.1 ± 11.6	8.0 ± 10.1	5.7 ± 9.9
SSH	ORSA4	$cm\ dec^{-1}$	−13.6 ± 22.6	−9.3 ± 15.3	−3.9 ± 18.8	**−21.1 ± 11.9**[a]	**−19.4 ± 9.4**[a]	−13.4 ± 13.5[a]	−1.7 ± 17.8	−1.1 ± 9.2	−4.9 ± 7.5	4.9 ± 11.6	4.1 ± 11.4	2.1 ± 10.2
SSH	GODAS	$cm\ dec^{-1}$	**10.6 ± 6.9**[a]	0.8 ± 5.9	0.6 ± 7.0	0.0 ± 5.8	−3.4 ± 4.9	0.1 ± 5.8	15.7 ± 19.3	−1.6 ± 6.2	−1.7 ± 7.7	***21.7 ± 7.7***[a]	3.7 ± 6.2	−0.3 ± 4.8
SSH	SODA	$cm\ dec^{-1}$	5.2 ± 11.5	2.5 ± 9.7	−1.6 ± 12.7	3.5 ± 11.9	−5.2 ± 9.3	−6.5 ± 10.0	0.8 ± 13.0	−1.3 ± 9.9	−4.5 ± 9.8	0.2 ± 9.7	−1.4 ± 8.6	−4.0 ± 9.8
VWCV	GODAS	$m\ mon^{-1}\ dec^{-1}$	**10.7 ± 5.8**[a]	−2.3 ± 5.8	−2.8 ± 6.5	**14.6 ± 5.5**[a]	**5.6 ± 3.5**[a]	1.8 ± 3.8	**−4.0 ± 3.6**[a]	3.5 ± 4.2	**4.5 ± 3.6**[a]	2.6 ± 3.9	−0.3 ± 5.0	2.2 ± 3.7

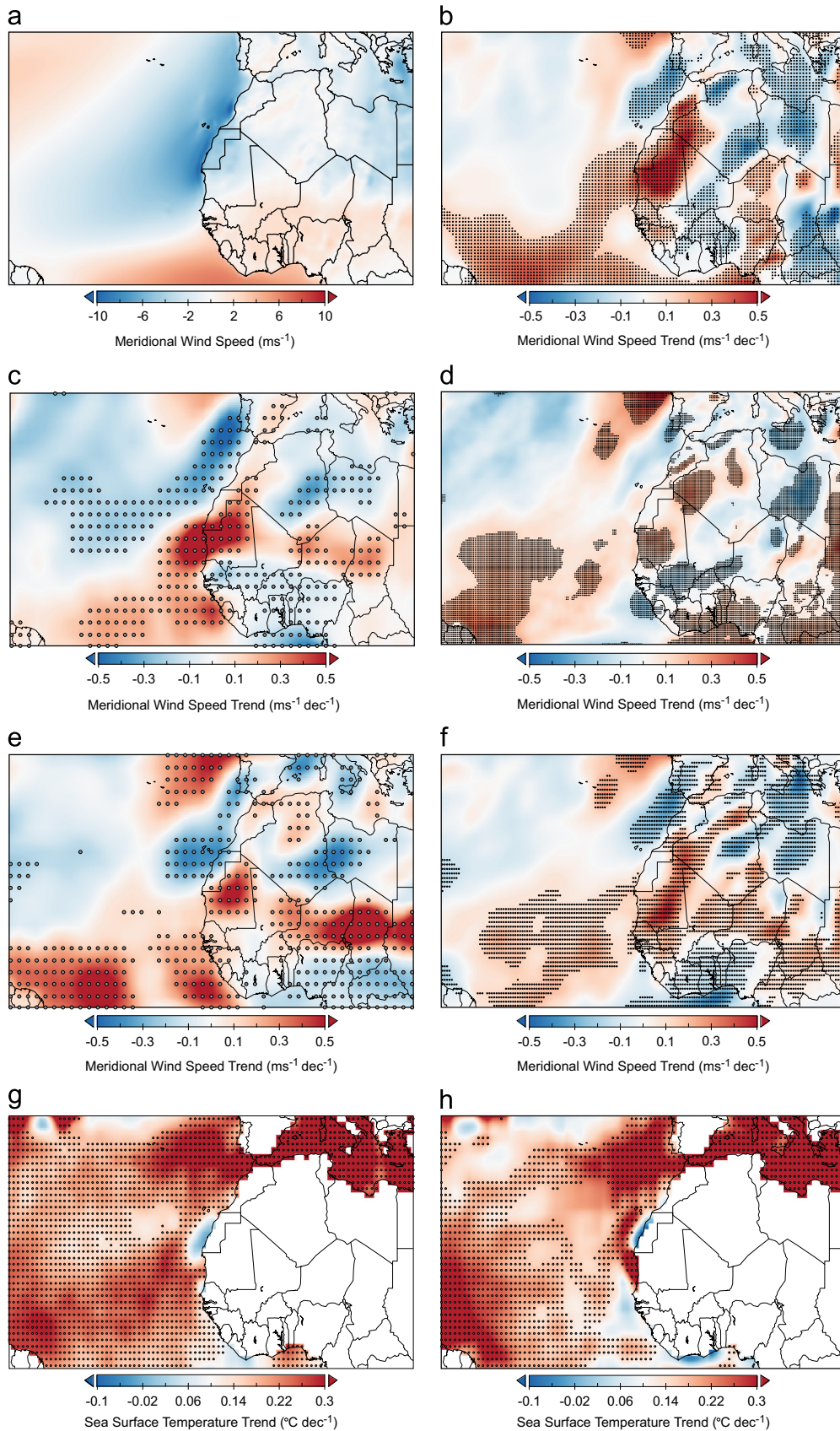[a] Indicates a statistically significant trend (Section 2).

Fig. 5. (a) Climatological summer (JJA) mean of meridional wind speed from the CFSR reanalysis (1981–2010) and the linear trend (1981–2012) of summer meridional wind speed for the (b) MERRA, (c) 20CR, (d) CFSR, (e) NCEP-DOE II and (f) ERA-I reanalysis datasets. A negative (positive) trend is associated with an equatorward (poleward) meridional wind anomaly. Also shown are the summer linear trends (1981–2012) in SST from the (g) HadISST and (h) OISST datasets. Stippling indicates significant trends ($p < 0.1$).
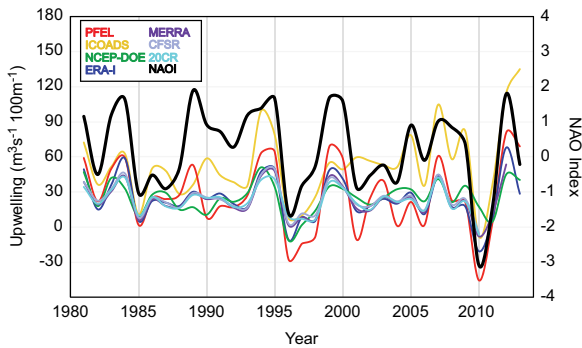
Fig. 6. Temporal evolution of winter (DJF) NAOI and winter UI^W indices across the Moroccan (26–35°N) upwelling zone.

decline across the Mauritania–Senegalese Zone and an increase across the two higher latitude zones. A more detailed spatial and temporal picture of the summer trend since 1981 is shown in Fig. 9b–d. Vertical velocity can seen to be increasing (i.e. water is more readily transported up to towards the surface) within a few grid points from the coastline north of 21°N and is decreasing (i.e. an increase in downward water column motion) southwards (Fig. 9b). This is reflected as well in Fig. 9c, which depicts the summer trends from the grid box closest to the coast, showing a significant increase from 22–30°N (with a gap around 25°N) and a negative trend south of 17°N. The Hovmöller diagram of annual summer anomalies (3-year running mean; Fig. 9d) highlights 1996–2004 and 2007–2012 as periods of generally enhanced vertical velocity transport (agreeing with stronger periods in the UI records), but for the equatorward region below 17°N, positive anomalies are most pronounced during 1980–1989, with strong negative anomalies during the post-2006 period.

3.3.3. Sea surface height

Prior to trend analysis in Table 2, we removed the seasonal cycle from all the SSH data and subtracted the regression of the global mean SSH on the SSH fields to serve as a crude removal of the general global SSH signal. Unfortunately, in addition to this crude removal potentially not fully removing the global signal, a trait shared across all six SSH measures is that the variability typically outweighs any trend estimates (Table 2) so significant trends are rare. However, we note for summer that the reanalysis trends north of 21°N (Table 2) are mostly negative (i.e. fitting in with the upwelling intensification hypothesis) but not significant, whereas altimetry trends are positive but also not significant.

4. Discussion

On the one hand, we find ample evidence for a summer upwelling increase north of 21°N for the 1981–2012 period, with significant trends in the ICOADS (wind), PFEL, NCEP-DOE II, HadISST, OISST and GODAS VWCV upwelling indices, as well as the TWI, and meteorological station wind speeds from Safi (and potentially Agadir and Nouakchott). There were supporting trends across the various UI's (more so across 26–35°N), including 10 m meridional wind speed (Fig. 5), SST and the GODAS and SODA SSH ocean reanalysis products (Table 2). The observations show a statistically significant increase north of 21°N and a generally significant decrease in upwelling-favorable winds south of 19°N (Table 2, Fig. 4). Such observations can be explained by invoking Bakun's (1990) upwelling intensification hypothesis, discussed in Section 1. During summer, under a warming climate a more rapidly warming African continent relative to the eastern North

Table 3
1981–2012 (or the longest temporal period available – see Table S1 for temporal data availability) winter (DJF) correlations between latitudinally averaged upwelling indices/indicators and the North Atlantic Oscillation (Station-based and Principal-Component based indices), East Atlantic Pattern, Atlantic Multidecadal Oscillation and El Niño Southern Oscillation. All time-series linearly detrended beforehand. Bold numbers and bold italics correspond to significant correlations at 95% and 99% respectively.

DJF	NAO (Station)	NAO (PC)	EA	AMO	ENSO
12–19N					
ICOADS (UI^W)	*0.52*	**0.36**	0.04	0.07	0.00
PFEL (UI^W)	*0.55*	*0.41*	−0.17	−0.02	−0.28
NCEP-DOE II (UI^W)	*0.47*	0.32	0.08	0.00	−0.20
ERA (UI^W)	**0.43**	0.30	0.04	−0.09	−0.02
MERRA (UI^W)	*0.53*	*0.43*	0.15	0.02	−0.18
CFSR (UI^W)	*0.46*	**0.40**	0.24	0.02	−0.13
20CR (UI^W)	**0.37**	0.34	0.28	0.00	−0.06
WASWIND (UI^W)	*0.67*	*0.53*	−0.21	0.16	−0.16
OISST (UI^ΔSST)	0.27	0.34	0.31	0.17	0.19
HADISST (UI^ΔSST)	0.17	0.24	0.26	0.22	0.13
ICOADS (UI^ΔSST)	0.09	0.08	0.24	0.08	−0.01
AVISO (SSH)	*−0.47*	−0.31	−0.05	−0.09	0.16
ORS4A (SSH)	−0.21	−0.11	0.06	0.03	0.03
GODAS (SSH)	0.10	0.23	0.10	0.22	0.11
SODA (SSH)	0.06	0.06	0.02	0.26	0.08
GODAS (VWCV)	−0.28	**−0.35**	−0.29	−0.13	−0.30
21–26N					
ICOADS (UI^W)	**0.44**	0.32	−0.21	−0.08	0.17
PFEL (UI^W)	*0.73*	*0.65*	0.00	0.28	−0.18
NCEP-DOE II (UI^W)	*0.76*	*0.63*	0.02	0.23	−0.19
ERA (UI^W)	*0.50*	0.32	0.03	−0.04	0.12
MERRA (UI^W)	*0.71*	*0.57*	0.01	0.17	−0.20
CFSR (UI^W)	**0.40**	0.29	0.28	0.14	−0.05
20CR (UI^W)	**0.41**	0.31	0.27	0.08	−0.05
WASWIND (UI^W)	*0.74*	*0.62*	−0.05	0.24	−0.18
OISST (UI^ΔSST)	−0.15	−0.07	0.07	0.01	−0.16
HADISST (UI^ΔSST)	*−0.46*	−0.33	−0.01	−0.19	−0.07
ICOADS (UI^ΔSST)	−0.26	−0.19	0.06	−0.27	−0.10
AVISO (SSH)	*−0.84*	*−0.72*	0.25	**−0.38**	0.21
ORS4A (SSH)	*−0.63*	*−0.49*	0.26	−0.16	0.18
GODAS (SSH)	*−0.49*	−0.33	0.06	−0.07	0.00
SODA (SSH)	**−0.43**	−0.24	0.10	0.30	−0.03
GODAS (VWCV)	**0.42**	0.24	−0.04	−0.06	−0.22
26–34N					
ICOADS (UI^W)	*0.57*	**0.45**	−0.14	0.12	0.14
PFEL (UI^W)	*0.81*	*0.70*	−0.12	0.30	−0.11
NCEP-DOE II (UI^W)	*0.86*	*0.75*	−0.19	0.32	−0.12
ERA (UI^W)	*0.62*	*0.47*	−0.13	0.10	0.18
MERRA (UI^W)	*0.84*	*0.73*	−0.12	0.27	−0.13
CFSR (UI^W)	*0.70*	*0.61*	0.13	0.26	0.02
20CR (UI^W)	*0.70*	*0.61*	0.10	0.26	−0.01
WASWIND (UI^W)	*0.81*	*0.72*	−0.25	0.29	−0.08
OISST (UI^ΔSST)	−0.25	−0.14	0.07	−0.07	−0.33
HADISST (UI^ΔSST)	−0.14	−0.09	0.08	0.01	*−0.49*
ICOADS (UI^ΔSST)	0.05	0.18	−0.04	0.15	*−0.41*
AVISO (SSH)	*−0.62*	**−0.48**	0.37	−0.13	0.17
ORS4A (SSH)	*−0.69*	*−0.55*	0.19	−0.17	0.09
GODAS (SSH)	*−0.56*	**−0.43**	0.26	−0.27	0.03
SODA (SSH)	*−0.63*	**−0.45**	0.18	0.00	0.00
GODAS (VWCV)	*0.84*	*0.70*	−0.15	0.33	−0.08

Atlantic Ocean will intensify the gradient between the continental low and the oceanic high pressures, enhancing onshore wind strength. Due to the Coriolis deflection, these winds will enhance equatorward alongshore wind strength, generally in the region around 21–35°N (i.e. the permanent annual upwelling regions), driving greater Ekman transport and upwelling. South of ~19°N poleward meridional winds are strengthened, favoring downwelling. This latitudinal divide is a function of the summer position of the Azores High/Inter-Tropical Convergence Zone (ITCZ), which makes the average alongshore/meridional wind component
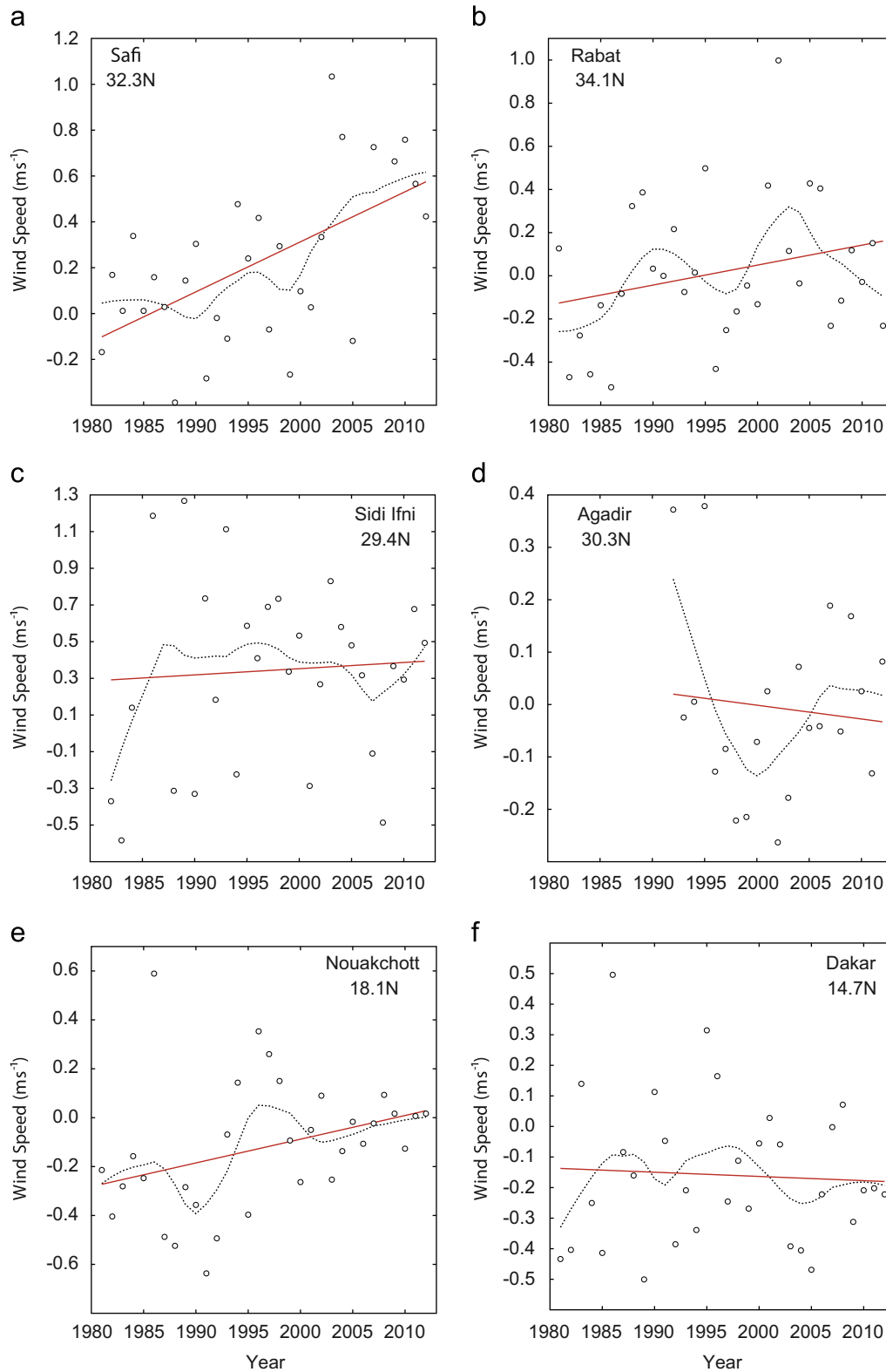
Fig. 7. Temporal evolution of summer wind speed anomalies (relative to the 1981–2010 base period) across six coastal meteorological stations situated along the NW African coastline (Fig. 1). Red lines indicate the linear trend across the entire period and dotted lines the 9-year loess trend. (For interpretation of the references to color in this figure legend, the reader is referred to the web version of this article.)

equatorward (poleward) across the permanent upwelling zones (Mauritania–Senegalese upwelling zone, (Fig. 5a)). A similar latitudinal divide has also been noticed in SST trends by Marcello et al. (2011). This alongshore wind speed intensification mechanism is augmented by the large scale northeast trade winds and

southwest West African monsoonal winds which again, reach a summer latitudinal divide at around ∼20°N.

Contrary to the supporting evidence for an upwelling intensification across the NW African coastline are differing lines of evidence that raise sufficient doubt as to whether or not the
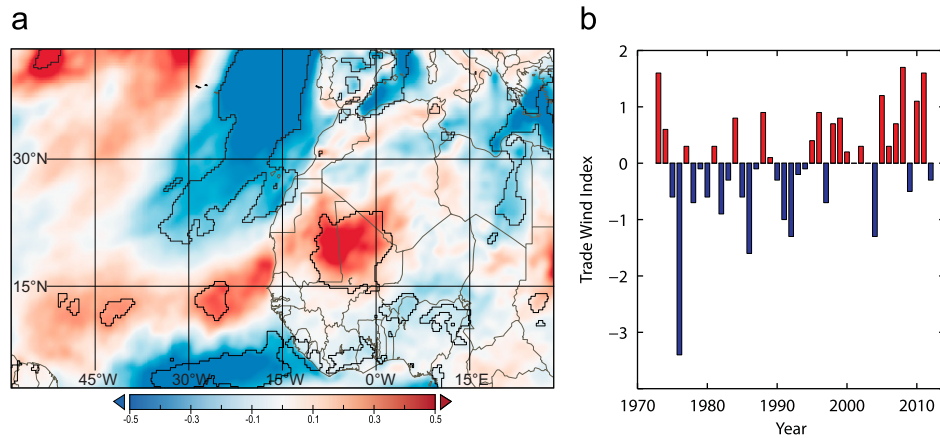
Fig. 8. (a) Linear regression of the summer TWI on 10 m meridional wind speed from the CFSR reanalysis (1981–2010), significant ($p < 0.1$) areas bounded by solid black lines and (b) the evolution of the summer TWI (based on the normalized SLP difference between the Azores and Cape Verde) from 1973 to 2012.
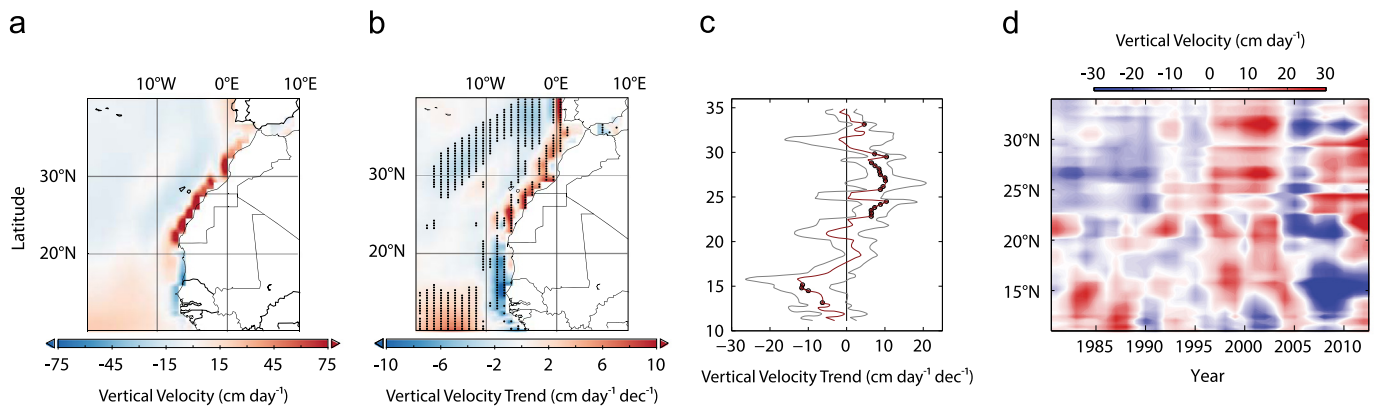

Fig. 9. (a) The summer (JJA) climatology and (b) linear trend of GODAS 50m vertical water column velocity across 1981–2012, stippling indicates significant trends ($p < 0.1$). Figure (c) displays the linear trend (by latitude) of the nearest available grid box adjacent to the coastline with circles indicating significant trends and gray lines the confidence intervals. Also shown (d) are the summer anomalies (3-year running average) of the coastal grid boxes.

supporting results can positively support a real trend. The main source of doubt is the general lack of a supporting reanalysis UI^W trend (Table 2, Fig. 4). Discrepancies between reanalysis and maritime and continental wind-speed trends have been demonstrated by several authors, with the common consensus appearing to be that reanalysis wind speeds are biased low (Smith et al., 2001; Wu and Xie, 2003; Vautard et al., 2010). Recently, Kent et al. (2013) highlighted how wind speeds in several datasets (including NCEP and ERA-I) suffer from a low wind speed bias (~ 1–2 ms^{-1}) at coastal locations when compared to the open ocean, offering further support for this idea. Thomas et al. (2008) attempted to remove the spurious positive bias in ICOADS wind-speed trends due to observational influences and identified that, since 1982, a real wind-speed trend is still likely, although they may not have accounted for every inhomogeneity. Narayan et al. (2010) encountered similar conflicting trends between reanalysis datasets and ICOADS when examining meridional wind speeds across the four eastern boundary currents, and gave greater credibility to the conclusions from the ICOADS dataset (but without an attempt to correct for bias). The PFEL indices offer another data source that is somewhat independent of ICOADS, as they are derived from the US Navy Fleet Numerical Meteorology and Oceanography (FNMOC) operational forecast model (NOGAPS, Goerss and Phoebus (1992)). The PFEL UI^W trends often exceed the ICOADS values (Table 2), highlighting the consistency of significant trends we see from the 'observational' indices as opposed to reanalysis. Fig. 5 illustrates that the trends in the observational UI^W (i.e. enhanced

equatorward (poleward) meridional wind north of (south of) $\sim 21°$N) are, in essence, represented in meridional reanalysis summer trends. However, reanalyses indicate a latitudinal divide in meridional trends around $\sim 25°$N which is slightly further poleward than the approximate climatological meridional 10-m wind-speed direction change (Fig. 5a). This disagreement arises because of the inclusion of the zonal wind component and coastline rotation in the UI^W calculation (meridional wind speed on its own serves as a good indicator but the UI^W will be more accurate).

We can attempt to validate the ICOADS trends by analyzing the WASWind dataset (Tokinaga and Xie, 2011b) and comparing ICOADS to winds derived from scatterometry (SeaWinds, Lungu et al., 2006). The WASWind dataset adjusts the ICOADS observations by correcting wind speeds for anemometer height changes, removing spurious Beaufort estimates and estimating wind speeds from wave height data and we find that across the CUE, the summer UI^W calculated from WASWind (not shown) across all latitudes displays a monotonic trend, suggesting that the ICOADS trend from 1981 to 2012 is positively biased. However we consider that the lack of WASWind trend is probably due to the course spatial resolution ($4°$), which makes it unlikely that coastal wind intensification would be picked up by the dataset. A comparison of ICOADS and SeaWinds summer evolution (UI^W) across the three upwelling zones is shown in Fig. 10. The SeaWinds magnitudes are generally weaker north of (stronger southwards) $21°$N, probably due to the ICOADS observations having a variable height but generally in the region of around ~ 25 m (Kent et al., 2007)
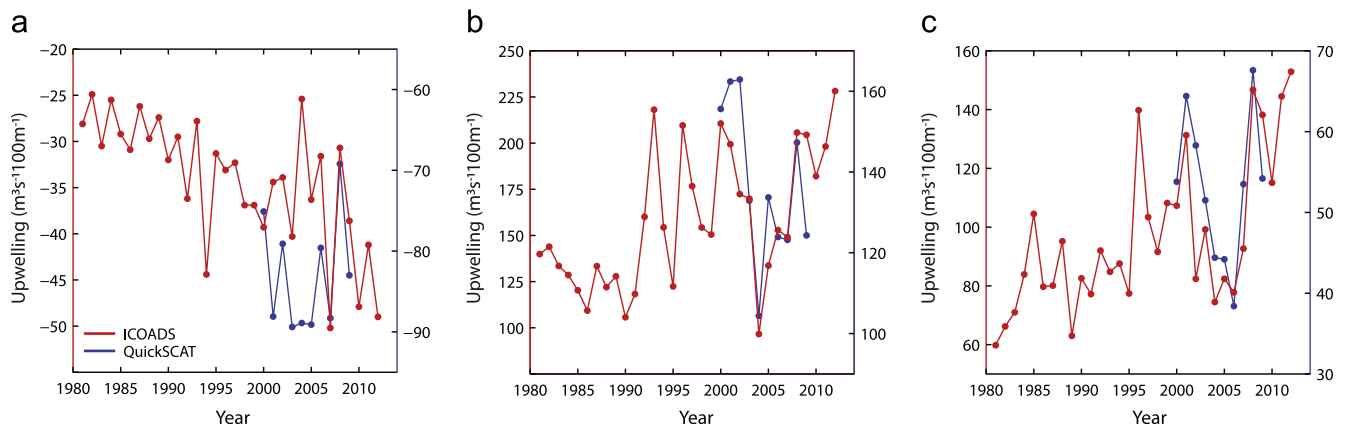
Fig. 10. A comparison of ICOADS and QuickSCAT calculated summer (JJA) UI^W values across the (a) Mauritania–Senegalese upwelling zone (12–19°N), (b) permanent upwelling zone (21–26°N) and (c) weak permanent upwelling zone (26–35°N).

compared to the 10 m SeaWinds. Fig. 10 shows that the SeaWinds matches ICOADS with reasonable agreement across 21–35°N but poorly across 12–19°N; however, with such a short temporal record the fit is partly subjective. Potential errors in the SeaWinds include signal degradation near the coast, due to rather variable surface roughness near the coastline and the land boundary and the (low) wind speed bias due to precipitation and clouds; yet the fit with ICOADS is encouraging and adds further support towards a coastal wind intensification.

Further evidence, which is potentially contrary to the upwelling intensification hypothesis, is a lack of significant wind-speed increase from near-coastal meteorological stations except at Safi (Fig. 7). However, land-based stations worldwide have a documented decrease in wind speed during the past four decades (Vautard et al., 2010) – attributed mainly to increasing surface roughness. It is possible such a signal contaminates our analyzed meteorological stations (and that being airport stations – are potentially poorly sited). However, the summer 1981–2012 wind speed trends are positive at four out of six stations and the trend at Agadir and Nouakchott are positive and significant when the anomalously high values (Section 3.3.1) early in the record are removed, leaving only Dakar (less than ideally suited on the Cape Vert Peninsula) displaying no long-term positive trend.

One final uncertainty is the discrepancy between altimetry and reanalysis SSH (Table 2). The summer climatological SSH means of the GODAS and SODA reanalyses and the altimetry data show a clear match. All three reflect the reduced SSH near the NW African coastline (Supplementary Fig. 1); however trend directions vastly differ. The two reanalyses indicate a summer reduction in SSH between ~23–31°N whereas the altimetry shows a ubiquitous increase across all latitudes. This may be due to the global SSH signal overriding any coastal process at a monthly scale in the altimetry data, hence why we crudely removed the global signal for SSH trends in Table 2. However, given the variability in the data, no significant trend emerges. As the ocean reanalyses all assimilate SSH, we speculate the difference is due to how the reanalyses incorporate altimetry observations and close the global freshwater budget. With ocean reanalysis, Boussinesq approximations are made (i.e. global ocean volume has to remain constant) which makes assimilation of a steric (changes from temperature and salinity) global trend problematic. The different models overcome this problem in different ways (Behringer, 2007; Carton and Giese, 2008; Balmaseda et al., 2013) and generally show good agreement (via root mean square error) with altimetry SSH in the Pacific, but not as good in the Atlantic. It is possible the reanalyses trends (which fit the upwelling intensification hypothesis) may be an artifact of less than perfect model SSH calculation/resolution in the

Atlantic (or the discrepancies in temporal period analyzed, (Supplementary Fig. 1)); this requires future investigation. However given the large variability of seasonal SSH trends and the relatively short time periods that SSH data are available across the NW African coastline (along with a lack of quality tide-gauge data and uncertainty of SSH at the coastal boundary), we suggest that this variable is not currently ideal for analyzing NW African upwelling.

Outside of summer, spring is the other season in which we intuitively would expect a potential UI increase (across all latitudes), but find generally insignificant/conflicting trends (Table 2). The NAO correlations with the various UI indices are strong in spring and autumn, but exceptionally strong in winter (Fig. 6; Table 3). This relationship is due to the strength of the Azores semi-permanent high-pressure system, which modifies trade wind strengths, and so the wind speed fields across the NW African upwelling zone. This is why the fixed NAO Azores–Iceland station based index displays generally stronger relationships than the PC-based version (Table 3). The EA pattern, which is a southward-shifted NAO-like oscillation, becomes prominent in spring and correlates with several of the weak upwelling zone indices in summer. Rather than this being an alternative pattern potentially explaining the variability in the UI, we feel it generally (during these seasons) serves as a reflection of the state/strength of the Azores High, which itself is most persistent during autumn–spring. As such, the main mode of variability across the Atlantic sector, which directly relates to the Azores High (represented by either the NAO/EA) can generally explain about 20–40% of the seasonal variability in the spring and autumn UI, 30–60% during winter and a likely insignificant amount of seasonal variability during summer (Table 3). A recently published study, which used ICOADS, WASWIND, NCEP, PFEL and ERA-40 winds, identified a weakening in upwelling across the CUE from 1967–2007 (Barton et al., 2013). However, the authors present only annual trends (we have identified that seasonal variation is strongly dependent on the NAO/EA) and truncate the time series to 2007 (the past 5 years significantly enhance the UI^W trends), potentially explaining a lack of summer intensification in their findings.

The AMO, which has been in its positive phase from ~1995 (Wang, 2011), may potentially have an effect on coastal upwelling by modifying SSTs around the NW African coastline (associated with its typical 'tri-pole' SST signal across the Atlantic Ocean). Generally, raw correlations between the AMO and our UI are ambiguous (Table 3); however, as the main time cycle of the AMO is roughly ~70 years, we cannot guarantee that it has no effect based solely on the correlations in Table 3. Additionally, the effects of ENSO are also likely limited, as direct correlations are rarely significant (Table 3).

Fig. 11 depicts the potential effect on summer upwelling across the NW African coastline in a globally warming world based on the
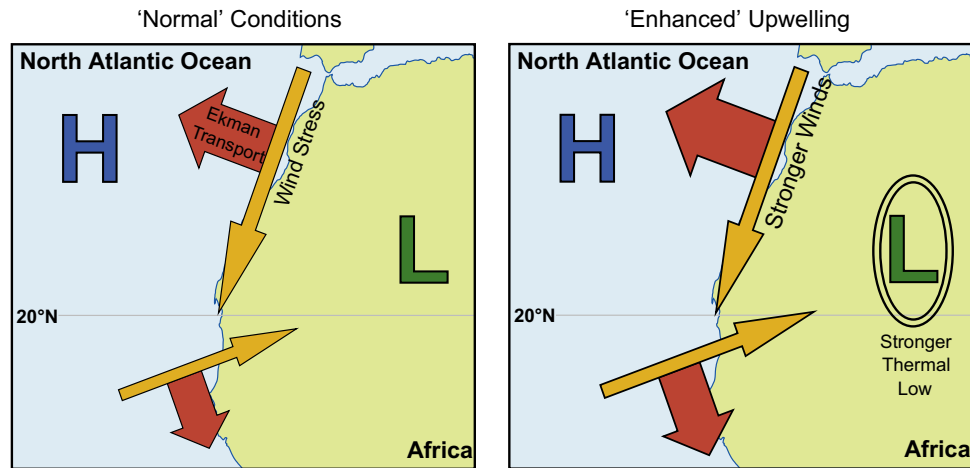
'Normal' Conditions   'Enhanced' Upwelling

Fig. 11. The upwelling intensification hypothesis (for summer, JJA), modified after Bakun et al. (2010). A thermal low surface pressure cell develops across the African continent as a result of the continent heating faster than the ocean. The comparatively higher pressures across the ocean results in airflow towards the continent which is deflected by the coriolis effect to the right, resulting in enhanced equatorward (poleward) alognshore winds across ~45–20°N (below 20°N). This latitudinal divide is a function of the mean position of the Intertropical Convergence Zone during summer, as such, the general wind patterns are from the NE above 20°N (the Trade Winds) and SW below 20°N. Figure (b) depicts the upwelling region in a globally warming world, with (assumed) more greenhouse gas emissions and water vapor across the region, which increases daytime heating and inhibits nighttime cooling – driving a stronger pressure gradient between atmosphere and ocean. This results in stronger winds across the region, which drives stronger than normal Ekman transport and increases coastal upwelling north of 20°N, and downwelling south of 20°N.

patterns found in our various UI. The mechanism in Fig. 11 applies to our period of study (1981–2012), but we would also expect, if global warming continues unabated, that this mechanism will intensify (i.e. Fig. 11b). Our findings reinforce the upwelling intensification hypothesis of Bakun (1990), whilst modifying the idea for the NW African coastline, across which a ubiquitous upwelling increase has not occurred due to the latitudinal divide in summer wind speed regimes. Generally, a consistent increase in wind speed brought about by the land–ocean pressure gradient results in an increase in coastal upwelling across 21–35°N (near-surface offshore winds) and increase in downwelling-favorable winds south of 19°N (near-surface onshore winds). The latter may be related to the 'recovery' in Sahel precipitation since the droughts of the 1970–80s (Nicholson, 2013), as increased onshore winds are consistent with a strengthening West African Monsoon, although this is one of many potential explanations. Additionally, under enhanced upwelling conditions, impacts on marine life can vary (Chavez and Messié, 2009; Bakun et al., 2010), as a direct upwelling increase does not necessarily equate to an increase in chlorophyll/primary production. In addition to biological constraints (mainly iron availability (Capone and Hutchins, 2013)), physical constraints such as the depth/size/slope of the continental shelf result in different upwelling regimes across the NW African coastline as the shelf properties can control how nutrients are recycled between periods of more intense upwelling and relaxation periods (Arístegui et al., 2009).

5. Conclusions

Trends in seasonal values of coastal upwelling across the NW African coastline were analyzed from 1981–2012. The different data sources used to characterize UI^W and $UI^{\Delta SST}$ provide very similar results for the mean fields (Fig. 2), and show the previously described spatial and temporal patterns of upwelling well – a permanent annual upwelling regime north of 21°N (which sometimes weakens/reverses around 30°N) and a seasonal regime south of 19°N (where downwelling conditions dominate during the summer months). However, trend directions often differ between observational and reanalysis datasets (Table 2). Focusing on summer (JJA), we found that the observational UI^W and $UI^{\Delta SST}$ favor an increase in upwelling across 21–35°N and increase in downwelling south of 19°N, a pattern generally supported by a separate analysis of 10-m meridional wind

speed trends. Reanalysis-derived UI^W support the trend increase across 26–35°N (the weak permanent upwelling zone) but appear mainly monotonic across the lower latitudes. Additionally, supporting proxy indices, which include wind speed data from six meteorological stations, the TWI (judged by its regression pattern on 10 m meridional wind speeds and its positive trend from 1973 onwards), vertical water column motion and SSH trends from ocean reanalyses, all offer further indication that the observational datasets' generalized wind speed increase across all latitudes (11–35°N) is real. Negative trends in summer coastal SST across the permanent upwelling zone (21–26°N) suggest that the impact of stronger winds is already clear across this part of the coastline.

The NAO is an extremely strong influence on non-summer upwelling magnitudes and inter-annual variability, especially in winter, where significant correlations are displayed across all latitudes (Table 3). The EA pattern (which reflects the Azores high strength as it is a southward-shifted NAO like dipole) correlates strongly with the UI^W in spring, illustrating the strong influence of the Azores high in all seasons but summer. An ENSO and AMO signal are absent in our analysis, but the latter's low frequency component may have a strong effect on NW Africa upwelling – a longer temporal UI^W record will help elucidate this in the future.

A modification of the Bakun upwelling intensification hypothesis based on the latitudinal divide between the NE trade winds and SW monsoon winds around 20°N (just for summer and for NW Africa) has been presented. As global warming intensifies, we would expect more favorable conditions for enhanced summer upwelling north of 20°N and an increase in downwelling-favorable winds equatorward. This will likely result in coastal SSTs displaying a reduced warming rate in comparison to the open ocean across the northern upwelling zones (21–35°N). The increase in onshore favorable winds across 12–19°N is possibly related to the minor recovery of the West African monsoon (compared to low values during the 1970–1980s), which may have assisted in a recent, partial recovery of rainfall for the Sahel region.

Appendix A. Supporting information

Supplementary data associated with this article can be found in the online version at http://dx.doi.org/10.1016/j.dsr.2014.01.007.

References

Alexanderson, H., 1986. A homogeneity test applied to precipitation data. J. Climatol. 6, 661–675.

An, S-I., Wang, B., 2001. Mechanisms of locking of the El Nino and La Nina Mature phases to Boreal winter. J. Climtol. 14, 2164–2176.

Arístegui, J., Barton, E.D., Álvarez-Salgado, X.A., Santos, A.M.P., Figueiras, F.G., Kifani, S., Hernández-León, S., Mason, E., Machú, E., Demarcq, H., 2009. Sub-regional ecosystem variability in the Canary Current upwelling. Prog. Oceanogr. 83, 33–48.

Bakun, A., 1990. Global climate change and intensification of coastal ocean upwelling. Science 247, 198–201.

Bakun, A., 1992. Global greenhouse effects, multi-decadal wind trends and potential impacts on coastal pelagic fish populations. ICES Mar. Sci. Symp. 195, 316–325.

Bakun, A., Nelson, C., 1991. The seasonal cycle of wind-stress curl in subtropical eastern boundary current regions. J. Phys. Oceanogr. 21, 1815–1834.

Bakun, A., Agostini, V.N., 2001. Seasonal patterns of wind-induced upwelling/downwelling in the Mediterranean Sea. Sci. Mar. 65, 243–257.

Bakun, A., Field, D.B., Redondo-Rodriguez, A., Weeks, S.J., 2010. Greenhouse gas, upwelling-favorable winds, and the future of coastal ocean upwelling ecosystems. Global Change Biol. 16, 1213–1228.

Balmaseda, M.A., Mogensen, K., Weaver, A.T., 2013. Evaluation of the ECMWF ocean reanalysis system ORAS4. Q. J. R. Meteorol. Soc. 139, 1132–1161.

Barnston, A.G., Livezey, R.E., 1987. Classification, seasonality and persistence of low-frequency atmospheric circulation patterns. Mon. Weather Rev. 115, 1083–1126.

Barton, E.D., Field, D.B., Roy, C., 2013. Canary current upwelling: more or less? Prog. Oceanogr 116, 167–178.

Behringer, D.W., 2007. The global ocean data assimilation system at NCEP. In: Proceedings of the 11th Symposium on Integrated Observing and Assimilation Systems for Atmosphere, Oceans, and Land Surface, Am. Meteorol. Soc., San Antonio, Tex.

Behringer, D.W., Xue, Y., 2004. Evaluation of the global ocean data assimilation system at NCEP: The Pacific Ocean. In: Proceedings of the Eighth Symposium on Integrated Observing and Assimilation Systems for Atmosphere, Oceans, and Land Surface, AMS 84th Annual Meeting, Washington State Convention and Trade Center, Seattle, Washington, pp. 11–15.

Borja, Á., Uriarte, Andrés, Valencia, V., Motos, L., Uriarte, Adolfo, 1996. Relationships between anchovy (Engraulis encrasicolus L.) recruitment and the environment in the Bay of Biscay. Sci. Mar. 60, 179–192.

Buishand, T., 1982. Some methods for testing the homogeneity of rainfall records. J. Hydrol. 58, 11–27.

Capone, D.G., Hutchins, D.A., 2013. Microbial biogeochemistry of coastal upwelling regimes in a changing ocean. Nat. Geosci. 6, 711–717.

Cardone, V., Greenwood, J., Cane, M., 1990. On trends in historical marine wind data. J. Clim 3, 113–127.

Carton, J.A., Giese, B.S., 2008. A reanalysis of ocean climate using simple ocean data assimilation (SODA). Mon. Weather Rev. 136, 2999–3017.

Castelao, R.M., Barth, J.A., 2006. Upwelling around Cabo Frio, Brazil: The importance of wind stress curl. Geophys. Res. Lett. 33, L03602.

Chavez, F.P., Messié, M., 2009. A comparison of eastern boundary upwelling ecosystems. Prog. Oceanogr. 83, 80–96.

Cheung, W.W.L., Watson, R., Pauly, D., 2013. Signature of ocean warming in global fisheries catch. Nature 497, 365–368.

Church, J.A., White, N.J., 2011. Sea-level rise from the late 19th to the early 21st century. Surv. Geophys. 32, 585–602.

Compo, G.P., Whitaker, J.S., Sardeshmukh, P.D., Matsui, N., Allan, R.J., Yin, X., Gleason, B.E., Vose, R.S., Rutledge, G., Bessemoulin, P., Brönnimann, S., Brunet, M., Crouthamel, R.I., Grant, A.N., Groisman, P.Y., Jones, P.D., Kruk, M.C., Kruger, A.C., Marshall, G.J., Maugeri, M., Mok, H.Y., Nordli, Ø., Ross, T.F., Trigo, R.M., Wang, X.L., Woodruff, S.D., Worley, S.J., 2011. The twentieth century reanalysis project. Q. J. R. Meteorol. Soc 137, 1–28.

Cropper T.E. and Hanna E., An analysis of the climate of Macaronesia, 1865–2012, Int. J. Climatol. Early View, http://dx.doi.org/10.1002/joc.3710, in press.

Dee, D.P., Uppala, S.M., Simmons, A.J., Berrisford, P., Poli, P., Kobayashi, S., Andrae, U., Balmaseda, M.A., Balsamo, G., Bauer, P., Bechtold, P., Beljaars, A.C.M., van de Berg, L., Bidlot, J., Bormann, N., Delsol, C., Dragani, R., Fuentes, M., Geer, A.J., Haimberger, L., Healy, S.B., Hersbach, H., Hólm, E.V., Isaksen, L., Kållberg, P., Köhler, M., Matricardi, M., Nally, A.P., Monge-Sanz, B.M., Morcrette, J.-J., Park, B.-K., Peubey, C., de Rosnay, P., Tavolato, C., Thépaut, J.-N., Vitart, F, 2011. The ERA-

Interim reanalysis: configuration and performance of the data assimilation system. Q. J. R. Meteorol. Soc. 137, 553–597.

Diffenbaugh, N.S., Snyder, M.A, Sloan, L.C., 2004. Could CO(2)-induced land-cover feedbacks alter near-shore upwelling regimes? Proc. Natl. Acad. Sci. USA 101, 27–32.

Falvey, M., Garreaud, R.D., 2009. Regional cooling in a warming world: Recent temperature trends in the southeast Pacific and along the west coast of subtropical South America (1979–2006). J. Geophys. Res 114, D04102.

Foster, G., Rahmstorf, S., 2011. Global temperature evolution 1979–2010. Environ. Res. Lett. 6, 044022.

Goerss, J.S., Phoebus, P.A., 1992. The Navy's Operational Atmospheric Analysis. Weather Forecast. 7, 232–249.

Gómez-Gesteira, M., Moreira, C., Alvarez, I., deCastro, M., 2006. Ekman transport along the Galician coast (northwest Spain) calculated from forecasted winds. J. Geophys. Res. 111, C10005.

Gómez-Gesteira, M., de Castro, M., Alvarez, I., Lorenzo, M.N., Gesteira, J.L.G., Crespo, A.J.C., 2008. Spatio-temporal upwelling trends along the Canary Upwelling System (1967–2006). Ann. NY Acad. Sci. 1146, 320–337.

Hagen, E., Feistel, R., Agenbag, J.J., Ohde, T., 2001. Seasonal and interannual changes in Intense Benguela Upwelling (1982–1999). Oceanol. Acta. 24, 557–568.

Hamed, K.H., Rao, A.R., 1998. A modified Mann–Kendall trend test for autocorrelated data. J. Hydrol. 204, 182–196.

Herbert, T.D., 2001. Review of alkenone calibrations (culture, water column, and sediments). Geochem. Geophys. Geosys 2 (2000GC000055).

Hsieh, W.W., Boer, G.J., 1992. Global climate change and ocean upwelling. Fish. Oceanogr. 1, 333–338.

Huyer, A., Smith, R., Paluszkiewicz, T., 1987. Coastal upwelling off Peru during normal and El Niño times, 1981–1984. J. Geophys. Res. 92, 14297–14307.

Kalnay, E., Kanamitsu, M., Kistler, R., Collins, W., Deaven, D., Gandin, L., Iredell, M., Saha, S., White, G., Woollen, J., Zhu, Y., Chelliah, M., Ebisuzaki, W., Higgins, W., Janowiak, J., Mo, K., Ropelewski, C., Wang, J., Leetmaa, A., Reynolds, R., Jenne, R., Joseph, D., 1996. The NCEP/NCAR 40-Year Reanalysis Project. Bull. Am. Meteorol. Soc. 77, 437–471.

Kanamitsu, M., Ebisuzaki, W., Woollen, J., Yang, S.-K., Hnilo, J.J., Fiorino, M., Potter, G.L., 2002. NCEP–DOE AMIP-II Reanalysis (R-2). Bull. Am. Meteorol. Soc. 83, 1631–1643.

Kent, E.C., Woodruff, S.D., Berry, D.I., 2007. Metadata from WMO publication No. 47 and an assessment of voluntary observing ship observation heights in ICOADS. J. Atmos. Ocean. Technol. 24, 214–234.

Kent, E.C., Fangohr, S., Berry, D.I., 2013. A comparative assessment of monthly mean wind speed products over the global ocean. Int. J. Climatol. 33, 2520–2541.

Lungu, T., Callahan, P.S., Dunbar, S., Weiss, B., Stiles, B., Huddleston, J., Shirtcliffe, G., Perry, K.L., Hsu, C., Mears, C., Wentz, F., Smith, D., 2006. QuikSCAT Science Data Product User's Manual. Version 3.0. ⟨ftp://podaac.jpl.nasa.gov/ocean_wind/quikscat/L2B/doc/QSUG_v3.pdf⟩.

Marcello, J., Hernández-Guerra, A., Eugenio, F., Fonte, A., 2011. Seasonal and temporal study of the northwest African upwelling system. Int. J. Remote Sens. 32, 1843–1859.

McGregor, H. V, Dima, M., Fischer, H.W., Mulitza, S., 2007. Rapid 20th-century increase in coastal upwelling off northwest Africa. Science 315, 637–639.

Miranda, P.M.A., Alves, J.M.R., Serra, N., 2012. Climate change and upwelling: response of Iberian upwelling to atmospheric forcing in a regional climate scenario. Clim. Dyn. 40, 2813–2824.

Mote, P.W., Mantua, N.J., 2002. Coastal upwelling in a warmer future. Geophys. Res. Lett. 29, 2138.

Narayan, N., Paul, A., Mulitza, S., Schulz, M., 2010. Trends in coastal upwelling intensity during the late 20th century. Ocean Sci. 6, 815–823.

Nicholson, S.E., 2013. The West African Sahel: a review of recent studies on the rainfall regime and its interannual variability. ISRN Meteorol 2013, 453521.

Nykjaer, L., Van Camp, L., 1994. Seasonal and interannual variability of coastal upwelling along northwest Africa and Portugal from 1981 to 1991. J. Geophys. Res. 99, 14197–14207.

Pardo, P., Padín, X., Gilcoto, M., Farina-Busto, L., Pérez, F., 2011. Evolution of upwelling systems coupled to the long-term variability in sea surface temperature and Ekman transport. Clim. Res. 48, 231–246.

Pauly, D., Christensen, V., 1995. Primary production required to sustain global fisheries. Nature 374, 255–257.

Payne, M.R., 2013. Climate change at the dinner table. Nature 497, 320–321.

Pérez-Brunius, P., Lopez, M., Pares-Sierra, A., Pineda, J., 2007. Comparison of upwelling indices off Baja California derived from three different wind data sources. CalCOFI Rep. 48, 204–214.

Pettitt, A., 1979. A non-parametric approach to the change-point problem. J. R. Stat. Soc. Ser. C – Appl. Stat. 28, 126–135.

Pickett, M.H., Paduan, J.D., 2003. Ekman transport and pumping in the California Current based on the U.S. Navy's high-resolution atmospheric model (COAMPS). J. Geophys. Res. 108, 3327.

Ramage, C., 1987. Secular change in reported surface wind speeds over the ocean. J. Clim. Appl. Meteorol. 26, 525–528.

Rayner, N., Parker, D., Horton, E., Folland, C., Alexander, L., Rowell, D., Kent, E., Kaplan, A., 2003. Global analyses of sea surface temperature, sea ice, and night marine air temperature since the late nineteenth century. J. Geophys. Res. 108, 4407.

Reynolds, R.W., Smith, T.M., Liu, C., Chelton, D.B., Casey, K.S., Schlax, M.G., 2007. Daily high-resolution-blended analyses for sea surface temperature. J. Clim. 20, 5473–5496.

Rienecker, M.M., Suarez, M.J., Gelaro, R., Todling, R., Bacmeister, J., Liu, E., Bosilovich, M.G., Schubert, S.D., Takacs, L., Kim, G.-K., Bloom, S., Chen, J., Collins, D., Conaty, A.,

da Silva, R., Gu, W., Joiner, J., Koster, R.D., Lucchesi, R., Molod, A., Owens, T., Pawson, S., Pegion, P., Redder, C.R., Reichle, R., Robertson, F.R., Ruddick, A.G., Sienkiewicz, M., Woollen, J., 2011. MERRA: NASA's modern-era retrospective analysis for research and applications. J. Clim. 24, 3624–3648.

Saha, S., Moorthi, S., Pan, H.-L., Wu, X., Wang, J., et al., 2010. The NCEP climate forecast system reanalysis. Bull. Am. Meteorol. Soc. 91, 1015–1057.

Santer, B.D., Wigley, T.M.L., Boyle, J.S., Gaffen, D.J., Hnilo, J.J., Nychka, D., Parker, D.E., Taylor, K.E., 2000. Statistical significance of trends and trend differences in layer-average atmospheric temperature time series. J. Geophys. Res. 105, 7337.

Santos, A.M., Kazmin, A., Peliz, A., 2005. Decadal changes in the Canary upwelling system as revealed by satellite observations: Their impact on productivity. J. Mar. Res. 63, 359–379.

Santos, F., DeCastro, M., Gomez-Gesteira, M., Alvarez, I., 2012. Differences in coastal and oceanic SST warming rates along the Canary upwelling ecosystem from 1982 to 2010. Cont. Shelf Res. 47, 1–6.

Saraceno, M., Strub, P.T., Kosro, P.M., 2008. Estimates of sea surface height and near-surface alongshore coastal currents from combinations of altimeters and tide gauges. J. Geophys. Res. 113, C11013.

Schwing, F.B., Farrell, M.O., Steger, J.M., Baltz, K., 1996. Coastal Upwelling Indices WestCoast of North America 1946-95, NOAA Technical Memorandum, NOAA-TM-NMFS-SWFSC-231. California.

Smith, S.R., Legler, D.M., Verzone, K.V., 2001. Quantifying uncertainties in NCEP reanalyses using high-quality research vessel observations. J. Clim. 14, 4062–4072.

Snyder, M.A., Sloan, L.C., Diffenbaugh, N.S., Bell, J.L., 2003. Future climate change and upwelling in the California Current. Geophys. Res. Lett. 30, 1823.

Sverdrup, H.V., 1938. On the process of upwelling. J. Mar. Res 2, 155–164.

Thiel, M., Macaya, E.C., Acuna, E., Arntz, W.E., Bastias, H., Brokordt, K., Camus, P.A., Castilla, J.C., Castro, L.R., Cortes, M., Dumont, C.P., Escribano, R., Fernandez, M., Gajardo, J.A., Gaymer, C.F., Gomez, I., Gonzalez, A.E., Gonzalez, H.E., Haye, P.A., Illanes, J.E., Iriarte, J.L., Lancellotti, D.A., Luna-Jorquerai, G., Luxoroi, C., Manriquez, P.H., Marin, V., Munoz, P., Navarrete, S.A., Perez, E., Poulin, E., Sellanes, J., Sepulveda, H.H., Stotz, W., Tala, F., Thomas, A., Vargas, C.A., Vasquez, J.A., Vega, J. M.A., 2007. The humboldt current system of northern and central Chile. Oceanogr. Mar. Biol. 45, 195–344.

Thomas, B.R., Kent, E.C., Swail, R., Berry, D.I., 2008. Trends in ship wind speeds adjusted for observation method and height. Int. J. Climatol. 763, 747–763.

Tokinaga, H., Xie, S.-P., 2011a. Weakening of the equatorial Atlantic cold tongue over the past six decades. Nature. Geosci. 4, 222–226.

Tokinaga, H., Xie, S.-P., 2011b. Wave- and anemometer-based sea surface wind (WASWind) for climate change analysis. J. Clim. 24, 267–285.

Uppala, S.M., Kållberg, P.W., Simmons, A.J., Andrae, U., Bechtold, V.D.C., Fiorino, M., Gibson, J.K., Haseler, J., Hernandez, A., Kelly, G.A., Li, X., Onogi, K., Saarinen, S., Sokka, N., Allan, R.P., Andersson, E., Arpe, K., Balmaseda, M.A., Beljaars, A.C.M., Berg, L.V-D., Bidlot, J., Bormann, N., Caires, S., Chevallier, F., Dethof, A., Dragosavac, M., Fisher, M., Fuentes, M., Hagemann, S., Hólm, E., Hoskins, B.J., Isaksen, L., Janssen, P.A.E.M., Jenne, R., Mcnally, A.P., Mahfouf, J.-F., Morcrette, J.-J., Rayner, N.A., Saunders, R.W., Simon, P., Sterl, A., Trenberth, K.E., Untch, A., Vasiljevic, D., Viterbo, P., Woollen, J., 2005. The ERA-40 re-analysis. Q. J. R. Meteorol. Soc., 131; , pp. 2961–3012.

van Oldenborgh, G.J., te Raa, L.A., Dijkstra, H.A., Phillip, S.Y., 2009. Frequency- or amplitude-dependent effects of the Atlantic meridional overturning on the tropical Pacific Ocean. Ocean Sci. 5, 293–301.

Vautard, R., Cattiaux, J., Yiou, P., Thépaut, J.-N., Ciais, P., 2010. Northern Hemisphere atmospheric stilling partly attributed to an increase in surface roughness. Nat. Geosci. 3, 756–761.

Wang, C., 2011. Atlantic multidecadal oscillation, in "State of the Climate in 2011". Bull. Am. Meteorol. Soc 93 (7), S137–S138.

Wang, C., Enfield, D., 2002. A further study of the tropical western hemisphere warm pool. J. Clim. 16, 1476–1493.

Wolter, K., Timlin, M.S., 2011. El Niño/Southern Oscillation behaviour since 1871 as diagnosed in an extended multivariate ENSO index (MEI.ext). Int. J. Climatol. 31, 1074–1087.

Woodruff, S.D., Worley, S.J., Lubker, S.J., Ji, Z., Eric Freeman, J., Berry, D.I., Brohan, P., Kent, E.C., Reynolds, R.W., Smith, S.R., Wilkinson, C., 2011. ICOADS Release 2.5: extensions and enhancements to the surface marine meteorological archive. Int. J. Climatol. 31, 951–967.

Wu, R., Xie, S.-P., 2003. On equatorial Pacific surface wind changes around 1977: NCEP–NCAR reanalysis versus COADS observations. J. Clim. 16, 167–173.